International
Progress Report

**IPR-09-14**

# Äspö Hard Rock Laboratory

## Äspö Task Force
## on Engineered Barrier System

## Modelling of THM-coupled processes for benchmark 2.1.1 and 2.1.2 with the code GeoSys/RockFlow

Thomas Nowak
Herbert Kunz

Federal Institute for Geosciences and
Natural Resources, Hannover, Germany

March 2009

**Svensk Kärnbränslehantering AB**
Swedish Nuclear Fuel
and Waste Management Co

Box 250, SE-101 24 Stockholm
Phone +46 8 459 84 00

Äspö Hard Rock
Laboratory

| Report no. | No. |
|---|---|
| IPR-09-14 | F89K |
| Author | Date |
| Thomas Nowak<br>Herbert Kunz | March 2009 |
| Checked by | Date |
| | |
| Approved | Date |
| Anders Sjöland | 2009-10-20 |

# Äspö Hard Rock Laboratory

## Äspö Task Force on Engineered Barrier System

## Modelling of THM-coupled processes for benchmark 2.1.1 and 2.1.2 with the code GeoSys/RockFlow

Thomas Nowak
Herbert Kunz

Federal Institute for Geosciences and
Natural Resources, Hannover, Germany

March 2009

*Keywords:* Task Force, Engineered Barrier System, Modelling, Bentonite, Buffer, Thermal, Hydraulic, Mechanical

# Abstract

In 2004 the Swedish Nuclear Fuel and Waste Management Co. (SKB) initiated the project “Task Force on Engineered Barrier Systems”. This project has the objectives to verify the ability to model THM-coupled processes (task 1) and gas migration processes (task 2) in the clay-rich buffer materials. The tasks are performed on the basis of appropriate benchmarks.

This report describes the final results for the modelling of the THM-benchmarks 2.1.1 (Buffer/Container Experiment) and 2.1.2 (Isothermal Test) with the code GeoSys/RockFlow. Both in-situ experiments were conducted in the Canadian Whiteshell Underground Research Laboratory (URL). An interim report (NOWAK 2008) documented the results of two axially symmetric models. This report documents the calculations of a laboratory experiment on the buffer material that is used as calibration for the hydraulic properties of the buffer material, the setting-up of a 3-D model of the URL for both ITT and BCE and the modelling results in comparison to measured values.

# Sammanfattning

2004 initierade Svensk Kärnbränslehantering AB, SKB, projektet ”Task Force on Engineered Barrier Systems”. Syftet med detta projekt är att verifiera möjligheten att modellera THM-kopplade processer (Task 1) och gasmigrationprocesser (Task 2) i lerbaserade buffertmaterial. Lämpliga laboratorie- och fältförsök ligger till grund för modelleringsuppgifterna.

Denna rapport beskriver de slutgiltiga resultaten av modelleringen av THM-kopplade processer för Task 2 (Benchmark 2.1.1, Buffer/Container Experiment, BCE och 2.1.2, Isothermal test, ITT) med hjälp av koden GeoSys / RockFlow. Båda in-situ experimenten utfördes i Whiteshell Underground Research Laboratory (URL) i Kanada. I en interimrapport (Nowak 2008) dokumenterades resultaten av två axialsymmetriska modeller. Denna rapport dokumenterar beräkningarna från ett laboratorieexperiment med buffertmaterialet som använts vid kalibrering av de hydrauliska egenskaperna hos buffertmaterialet, framtagande av en 3D-modell för underjordslaboratoriet för både ITT och BCE och modelleringsresultaten jämförda med uppmätta värden.

# Contents

# 1 Introduction

Modelling coupled thermal, hydraulic, mechanical, and chemical processes is of importance for the investigation of different concepts for final repositories. The radioactive waste heats the surrounding system of engineered and geological barriers, and this process shows strong interactions with hydraulic, mechanical, and chemical processes.

In many concepts for final repositories clay-rich materials play an important role as a technical barrier. Due to adsorption of water into the clay mineral lattice these materials are capable of swelling. Changes in water saturation of this technical barrier are caused on the one hand by evaporation of water due to the heat generated by the waste, on the other hand by water from the host rock infiltrating into the technical barrier. The ability to understand and model these reverse processes is of special importance for the performance of a final repository for high active waste in crystalline rock and clay.

Several in-situ experiments with clay-rich materials as buffer material were conducted in underground research laboratories in crystalline rock. The data gained by these experiments (i.e. temperature, relative humidity, total stress) put the numerical tools to the test that are going to be used for the calculation of a repository layout. BGR uses the code GeoSys/RockFlow (GS/RF) for repository layouts in crystalline rock and clay(-stone). This code proved to be suitable for modelling the behaviour of clay-rich materials (see for example NOWAK 2007, SHAO et al. 2008).

This report describes the final results for the modelling of two in-situ experiments that were chosen as benchmarks (BM) in the project "Task Force on Engineered Barrier Systems" (chapter 4.2); an interim modelling report for these benchmarks documented the results from axially symmetric models (NOWAK 2008). Both in-situ experiments were performed in the Underground Research Laboratory (URL) of Atomic Energy of Canada Ltd. (AECL) to investigate a repository layout that consists of a horizontal array of waste-emplacement rooms at nominal depths of 500 to 1000 m in plutonic rock of the Canadian Shield (chapter 3.2 and 3.3). In this layout used nuclear fuel is stored within containers in boreholes drilled in the floor of emplacement rooms. The containers are positioned vertically within these boreholes (in-floor borehole emplacement method) (MAAK et al. 2005). The containers are to be isolated by repository sealing systems that include clay-rich buffer and backfills. These barriers are supposed to limit the rate of movement of contaminants, if any are released from the containers.

A bentonite-sand buffer material – as it was used in identical composition in these two in-situ experiments – is one of the engineered materials that may be placed around the waste container. Laboratory experiments had been performed with this bentonite-sand buffer (chapter 3.1), and the measured data from one of these experiments (specimen H-064-2) were taken to calibrate the behaviour of that mixture in the numerical model (chapter 4.1). In the modelling work described in this report it was especially featured to use one set of hydraulic parameter values for modelling both the laboratory experiment and the in-situ experiments. This approach limits the possibilities to match the measured data in the calculation by parameter value fitting.

The governing equations of the code can be found in NOWAK (2007).

# 2 Recent Development of Numerical Code GeoSys/RockFlow and the Pre- and Postprocessing Tool GINA

As prerequisite for setting-up 3-D models an appropriate tool for mesh generation is needed. Taking BM 2.1.1 and 2.1.2 as exemplary application an interface from GINA (BGR) to the mesh generator TetGen from the Weierstrass Institute for Applied Analysis and Stochastics (SI & GAERTNER 2005) was prepared. This programme needs as input a geometric description of surfaces; volumes are recognized by the programme itself in case that surfaces form a closed body. This feature is very helpful in the field of geotechnical application; consider for example the layout of the BCE with the heater inside the sand mantle which again is surrounded by the buffer. The mesh density can be controlled easily by volume constraints for the elements of a material (or volume, respectively).

The most important feature of GS/RF for coupled calculations on a large scale is the parallelization of the code which was used for the calculations documented in this report. The FEM scheme is partitioned by a priori domain decomposition and then assigned to the according CPU nodes concurrently. The domain decomposition of a mesh only uses the information of the mesh topology. Two principles of the decomposition are followed, namely to build sub-domains with little difference of the number of elements (that brings computational load balance) and to make border nodes as few as possible (thus reducing inter-processor communication). Parallelization is achieved by simultaneously assembling liner equation systems in sub-domains and obtaining the overall solution with a sub-domain linear solver (parallel biconjugate gradients stabilized method (BiCGStab) with Jacobi preconditioner). The present parallelization method is implemented in an object-oriented way using message passing interface (MPI) instructions for inter-processor communication. This feature is still object of further improvement, see for example KALBACHER et al. (2008).

Minor changes in the THM-coupling by material functions and governing equations are reported in chapter 4.2.

# 3 Experiments

## 3.1 Laboratory Tests on the Bentonite-Sand Buffer

In both in the Buffer/Container Experiment (BCE, BM 2.1.1) and the Isothermal Test (ITT, BM 2.1.2) a bentonite-sand mixture (50:50) was used as the buffer material. As part of the exercise to evaluate numerical tools for use in predicting system evolution, the participants were given two laboratory experiments to calibrate their models for water uptake and saturation.

### 3.1.1 Relationship Suction – Water Content

One of the primary relationships needed for predicting the THM-evolution of a clay-based barrier material is the relationship between suction and water content for the buffer. This had been previously determined by laboratory measurements on the materials tested in the BCE and ITT. The region of particular interest in this study is for values of dry density around the in-situ value for the BCE and the ITT (1720 kg/m$^3$ and 1730 kg/m$^3$, respectively). Figure 3-1 shows the measured values together with some approximations generated by curve-fitting functions. The initial water content of the buffer in BCE and ITT was 17.5% and at the densities considered in these experiments the maximum (gravimetric) water content achievable (full saturation) is approximately 20.9%. It should be noted that this value is an estimate only and is based on assumptions regarding the mineralogical composition (particle density) of the buffer components.

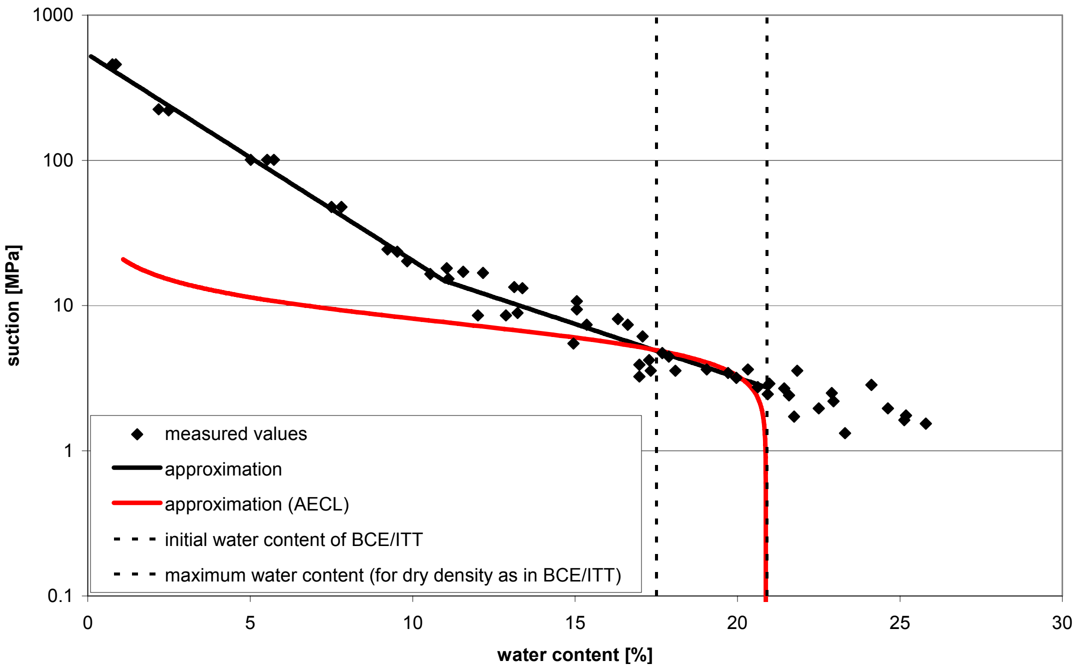

***Figure 3-1:*** *Suction – water content relationship for buffer material (after WAN et al. 1995).*

The suction – water saturation relationship that had been used by AECL for modelling the BCE is plotted into figure 3-1 in terms of gravimetric water content (red line). The corresponding equation is as follows:

$$S_r = \left[ 1 + \left( \frac{s}{P_0} \right)^{\frac{1}{1-\beta_1}} \right]^{-\beta_1} \qquad (1)$$

with

$S_r$: water saturation

$s$: suction

$P_0$: gas entry pressure, $P_0 = 7.0$ MPa

$\beta_1$: shape parameter, $\beta_1 = 0.73$

This approximation is close to the black line of best fit (in linear – logarithmic plot) through the measured suctions for the range of water content from the initial state of BCE/ITT with a water content of 17.5% to the maximum water content of about 20.9%.

### 3.1.2 Water Uptake Test

A second major consideration when doing numerical simulations is the relationship between degree of saturation and water movement through, or into the material being examined. A bench-scale test was used to evaluate this relationship for the range of water content of relevance in this study. The initial dry density of the sand-bentonite buffer material tested in the laboratory was 1700 kg/m$^3$ and its initial water saturation is 82.8%. At the outflow end of the volumetrically confined specimen (length: 43.5 mm; diameter: 50 mm) a dry stainless steel filter stone at atmospheric pressure was present. At the inflow end, water pressure was increased stepwise to get different hydraulic gradients along the specimen. From the measured inflow rates, average water saturation for the whole specimen was calculated, see figure 3-2.

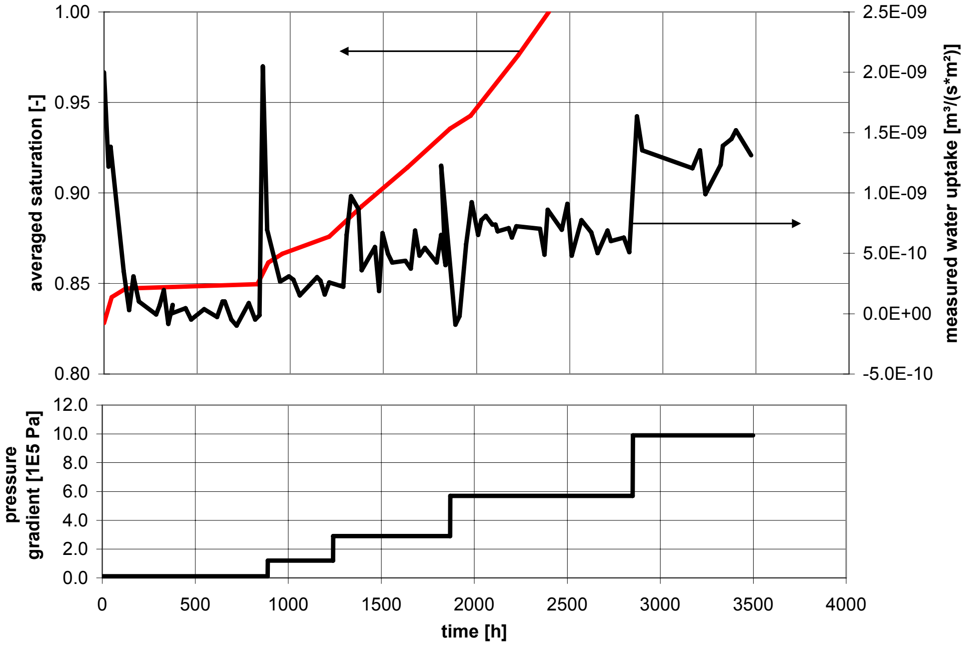

***Figure 3-2:*** *Water uptake test on bentonite-sand buffer material (data from AECL).*

The evolution of averaged saturation shows clearly a dependence on the applied pressure gradient. When full water saturation is reached (after roughly 2500 hours) the permeability value of this material can be defined at about $5 \cdot 10^{-20}$ $m^2$ using analytical equations. It should be noted that permeability values and relationships in the description of this task are based on best-fit relationships generated from extensive data bases. The individual values within this data base vary considerably (see figure 3-3) making a value for permeability an approximation only and numerical simulations need to examine the sensitivity of a range of value on their output.

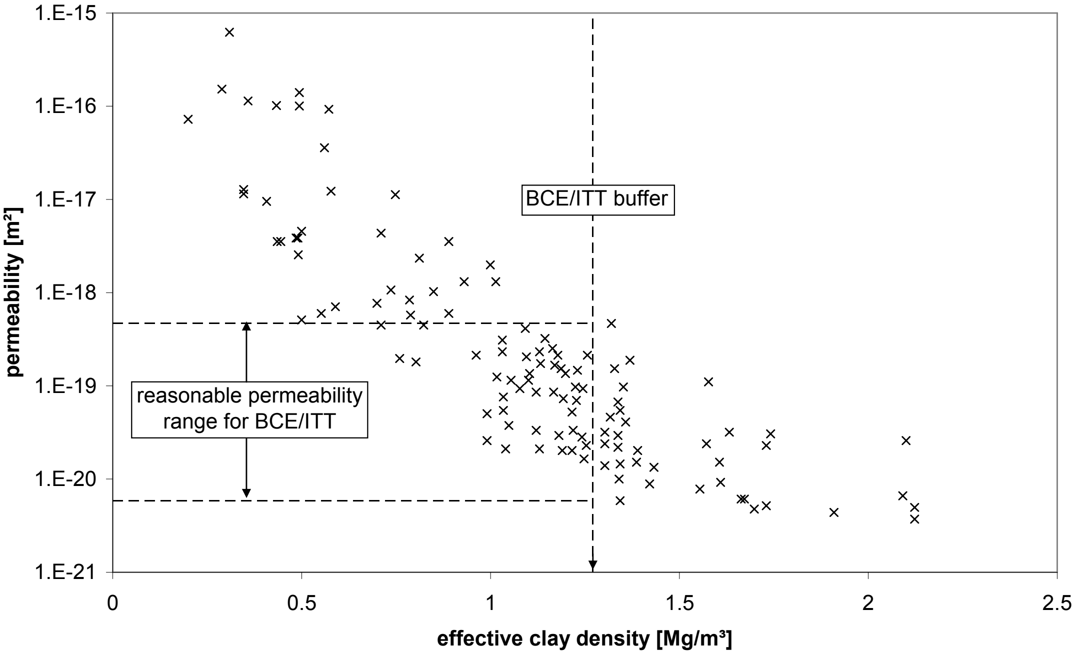

***Figure 3-3:*** *Permeability range for bentonite-sand buffer material (data from AECL).*

## 3.2 Buffer/Container Experiment

As BM 2.1.1 the Buffer/Container Experiment (BCE) was chosen which investigates how the heat from used fuel affects the performance of the dense bentonite-sand buffer. The BCE was carried out on the 240 Level of the URL, approximately 240 m below the surface, see figure 3-4.

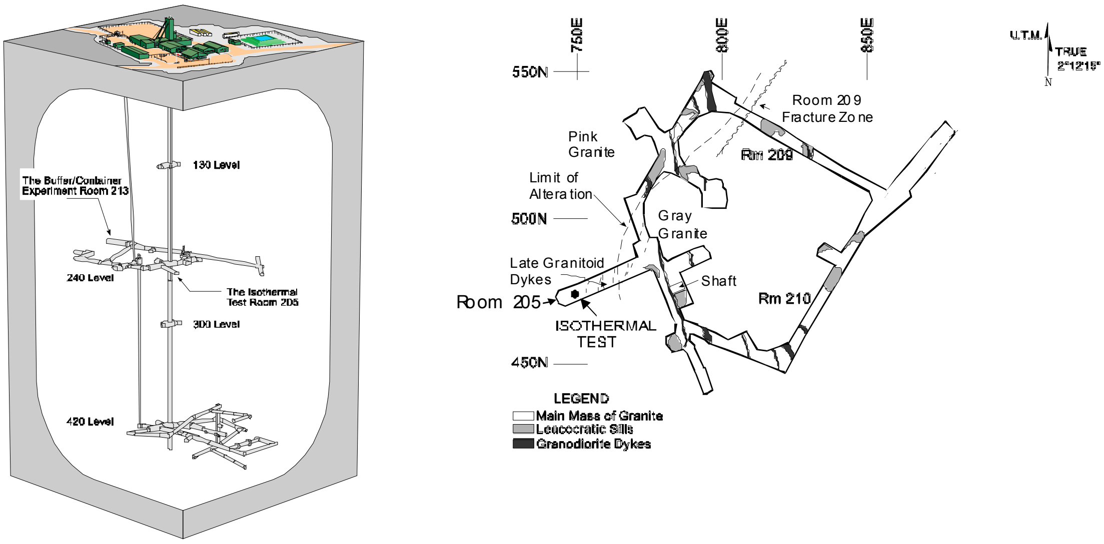

***Figure 3-4:*** *Overview of Whiteshell URL (pictures from AECL).*

At the experiment room (room 213), the rock is essentially an unfractured, homogeneous, grey granite. The BCE consisted of an electric heater installed in buffer in an in-floor borehole (depth: 5 m; diameter: 1.24 m), see figure 3-5. A layer of sand (thickness: 0.05 m) was installed between the heater and the surrounding buffer. A layer of backfill (gravel-sand-clay mixture, thickness: 1 m) was installed in the upper part of the emplacement borehole, above the buffer, and below the cell cap and reaction frame. The backfill consisted of 75 wt-% well-graded gravel aggregate and 25 wt-% glaciolacustrine clay. In terms of dry weight the clay used in the backfill was a mixture of 75 % illitic clay with 25 % sodium bentonite from Avonlea, Saskatchewan (GRAHAM et al. 1997). This means that the overall bentonite content of the backfill was only 6.25 wt-%, when translates to a smectite content of approximately 5 wt-%.

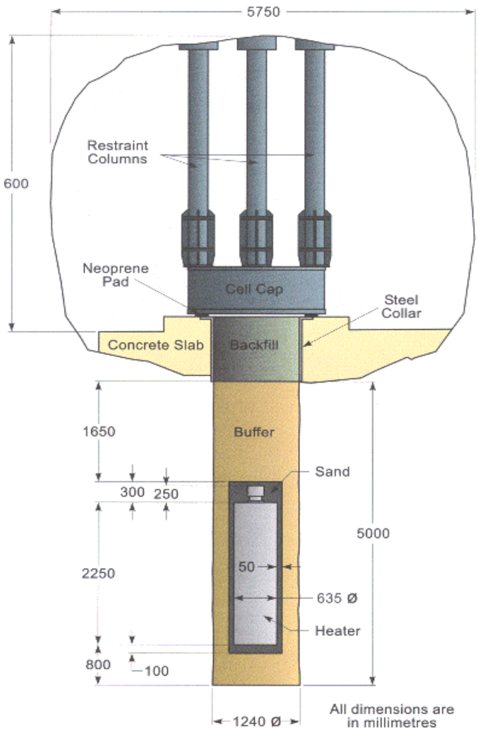

***Figure 3-5:*** *Construction layout of the BCE (after GRAHAM et al. 1997).*

The BCE consisted of a series of discrete phases:

- Excavation of the experiment room between (June 1989 – September 1989)
- Phase A (15/05/1990 – 13/05/1991):
  Drilling the emplacement borehole and monitoring the effect on water pressures, temperatures and hydraulic influxes in defined sections of the borehole.
- Phase B (13/05/1991 – 13/09/1991):
  Installation of the buffer, backfill, heater and instrumentation in the borehole.
- Phase C (13/09/1991 – 20/11/1991):
  A baseline monitoring period to allow temperatures, swelling and hydraulic pressures to stabilize.
- Phase D (20/11/1991 – 05/05/1994):
  A heating period, with power supplied to the heater for a total of 896 days (the heater power was 1000 W for the first 26 days and thereafter the heater power was increased to 1200 W).
- Phase E (05/05/1994 – 13/05/1994):
  A decommissioning phase in which the backfill, buffer, heater and instrumentation were removed from the emplacement borehole.
- Phase F (13/05/1994 – December 1995):
  A follow-up period after the experiment during which water pressures and temperatures in the host rock continued to be monitored.

The measured values are documented in the chapter for the modelling calculations as reference.

## 3.3 Isothermal Test

As BM 2.1.2 the Isothermal Test (ITT) was chosen which allows for a comparison of the buffer behaviour in comparison to the BCE under isothermal conditions. The ITT was carried out on the same level of the URL as the BCE, compare figure 3-4. At the experiment room (room 205) the rock has essentially the same properties as described for the BCE. Like the BCE the ITT was installed in an in-floor borehole (depth: 5 m; diameter: 1.24 m). The buffer material was compacted in situ into the bottom 2 m of the borehole. A 1.25-m-thick concrete plug overlaid the buffer to provide a vertical restraint against swelling, see figure 3-6.

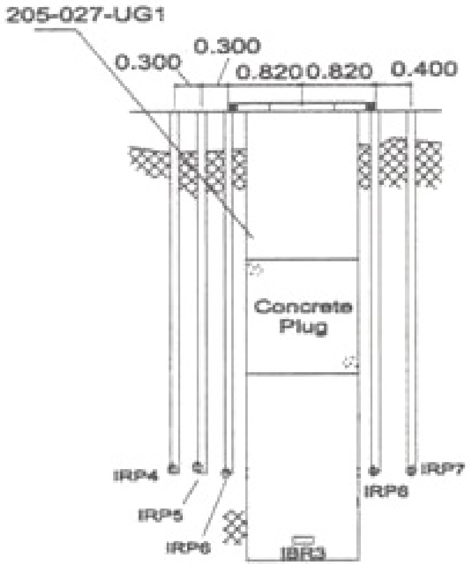

***Figure 3-6:*** *Construction layout of the ITT (picture from AECL).*

The ITT consisted of a series of discrete phases:

- Excavation of the experiment room:
  Ending in March 1989, assumed start in December 1988
- Phase 1 (March 1989 – September 1992):
  Drilling the emplacement borehole and monitoring the hydraulic influx for a period of 54 day from 05/03/1992 to 27/04/1992.
- Phase 2 (22/09/1992 – 10/02/1997):
  Installation of buffer, concrete plug and instrumentation in the borehole, then monitoring.

The measured values are documented in the chapter for the modelling calculations as reference.

# 4 Calculations

## 4.1 Water Uptake Test

Using the data from the water uptake test, two-phase flow calculations were performed for the examination of the sensitivity of following hydraulic parameters: suction – water content relationship (chapter 4.1.1), permeability (chapter 4.1.2), and finally water saturation – relative permeability relationship (chapter 4.1.3). Figure 4-1 shows the model and exemplary the saturation distribution in the model after 1000 hours for a permeability of $5 \cdot 10^{-20}$ $m^2$ and a van Genuchten parameter of 0.04 (compare chapter 4.1.3, figure 4-4).

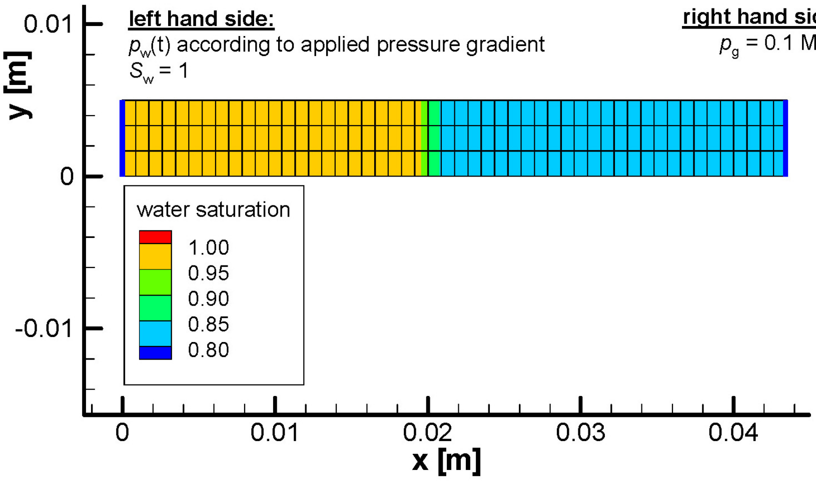

***Figure 4-1:*** *2D-model of water uptake test.*

Vapour flow was not taken into account in these calculations but given the high degree of saturation, this is not likely to have a discernible effect on the results. For comparison the calculation results for averaged water saturation are plotted in the following diagrams with blue symbols; measured averaged saturation (red line) was calculated from the measured water uptake (black line).

### 4.1.1 Calculations with varying suction – water content relationships

The permeability was fixed in these calculations at a value of $5 \cdot 10^{-20}$ $m^2$. The van Genuchten shape parameter of the water saturation – relative permeability relationship was set to 0.3. With the approximation of suction – water content relationship provided by AECL (red line in figure 3-2) the calculation gives a nearly saturated specimen after roughly 200 hours (blue diamonds, see figure 4-2). When the suction values are reduced by a factor of 10, calculated saturation time is roughly 1600 hours (blue squares). When suction values are reduced by a factor of 100, calculated saturation time is similar to the experimental result (red line) of roughly 2500 hours (blue triangles), and in this case the evolution of the calculated averaged water saturation nearly coincides with the saturation calculated from the measured water uptake (black line). These reductions of suction are a purely hypothetical approach, because measured suction values were higher (compare figure 3-1).

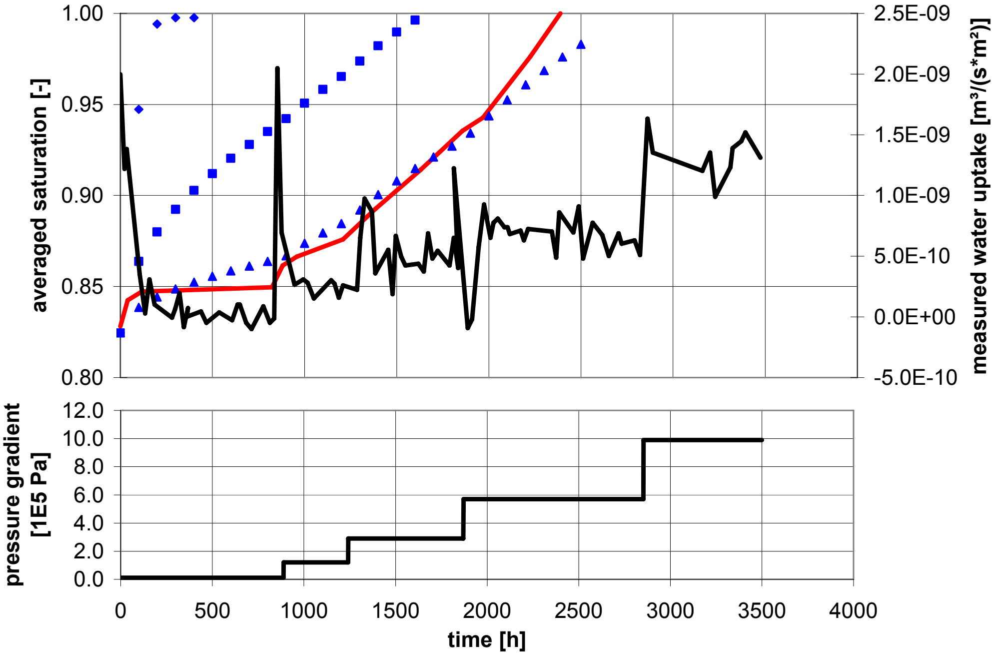

***Figure 4-2:*** *Comparison of measured and calculated evolution of averaged saturation within the whole specimen, variation of the suction – water content relation.*

### 4.1.2 Calculations with varying permeability

The suction – water content from AECL (red line in figure 3-2) was fixed in these calculations. The van Genuchten shape parameter of the water saturation – relative permeability relationship was set to 0.3. With a permeability of $5 \cdot 10^{-20}$ $m^2$ the calculation gives a saturation time of roughly 200 hours (blue diamonds, see figure 4-3). When the permeability value is reduced to $1 \cdot 10^{-20}$ $m^2$, calculated saturation time is roughly 1100 hours (blue squares). When the permeability value is reduced further to $4 \cdot 10^{-21}$ $m^2$, calculated saturation time is roughly 2500 hours (blue triangles). The evolution of the overall water saturation differs significantly from the saturation that was calculated from the measured water uptake.

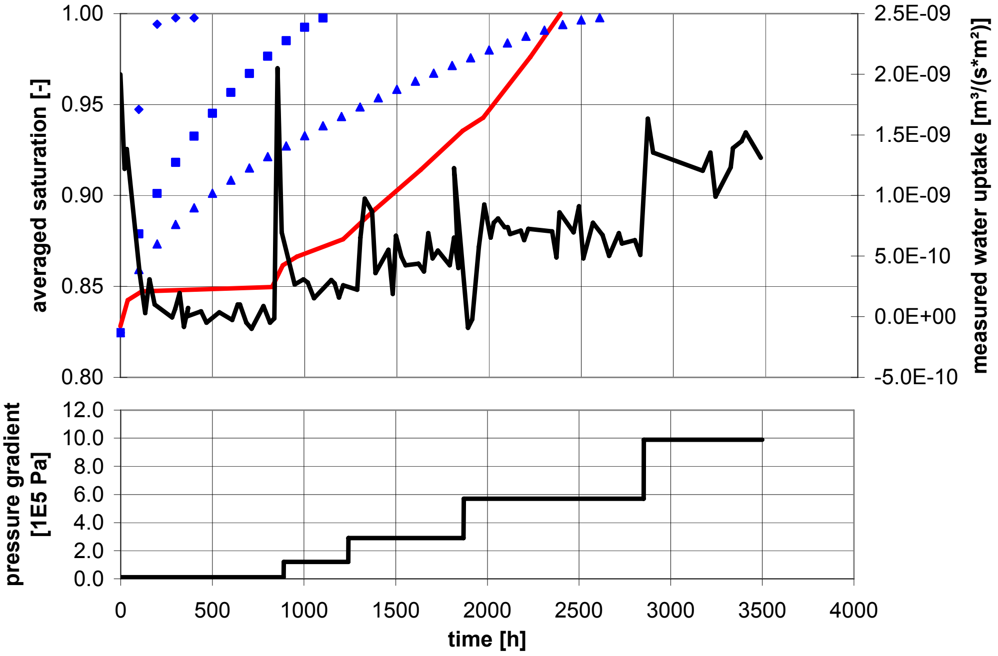

***Figure 4-3:*** *Comparison of measured and calculated evolution of averaged saturation within the whole specimen, variation of the permeability value.*

### 4.1.3 Calculations with varying water saturation – relative permeability relationships

The last series of calculations was performed to examine the effect of varying the van Genuchten shape parameter of the water saturation – relative permeability relationship:

$$k_r = S_r^{1/2}\left[1-\left(1-S_r^{1/\beta}\right)^{\beta}\right]^2 \qquad (2)$$

with

$k_r$: relative permeability for water

$\beta$: shape parameter

The permeability value was set to $5 \cdot 10^{-20}$ m$^2$ (analytical solution of flow through the specimen) and the suction – water content relationship was as approximated by AECL to the measured values (compare figure 3-1). With a shape parameter of 0.06 the calculation gives a saturation time of roughly 2000 hours (blue diamonds, see figure 4-4). When the shape parameter is 0.04, calculated saturation time is roughly 2600 hours (blue squares). When the shape parameter is reduced further to 0.02 (blue triangles) the specimen does not saturate within the duration of the experiment. The evolution of the averaged water saturation differs from the integral saturation that was calculated from the measured water uptake. In figure 4-5 the relative permeability for water is plotted vs. water saturation for the given values of the van Genuchten shape parameter.

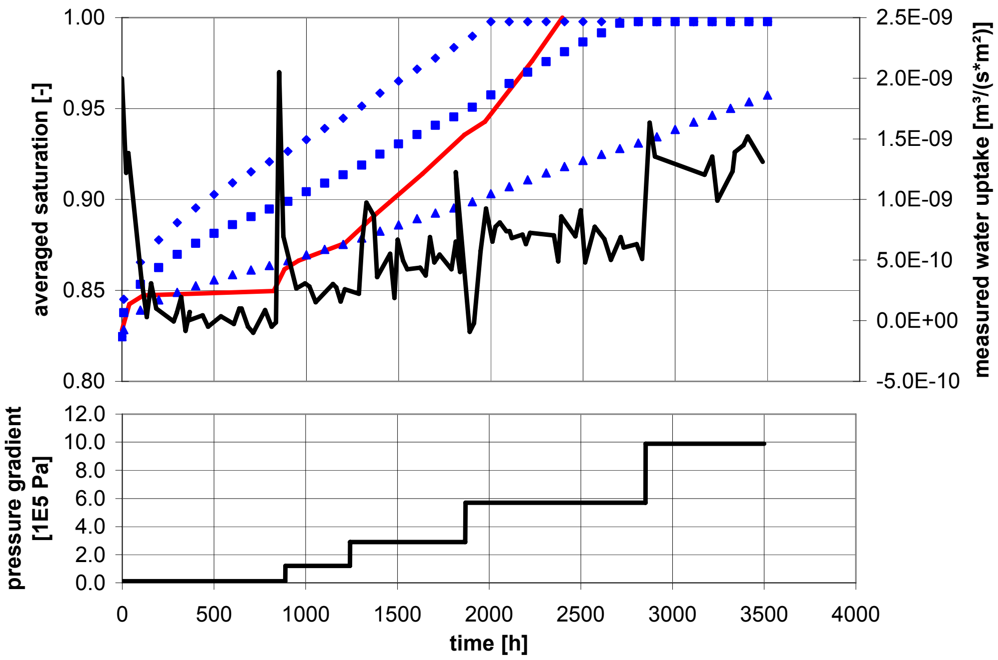

*Figure 4-4:* *Comparison of measured and calculated evolution of averaged saturation within the whole specimen, variation of the van Genuchten shape parameter of relative permeability – water saturation relationship.*

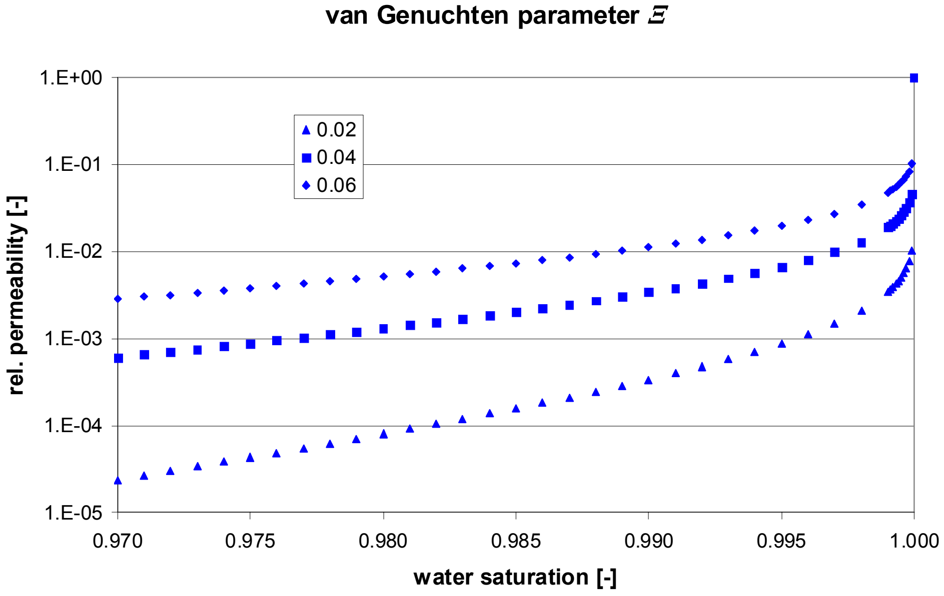

*Figure 4-5:* *Relative permeability for water vs. water saturation for different values of the van Genuchten parameter.*

### 4.1.4 Discussion

The calculations with varying suction – water content relationships were performed with 0.3 for the van Genuchten shape parameter for relative water permeability as suggested by AECL. When the suction is reduced by a factor of 100 the measured and calculated times for full averaged saturation agree well and also the evolution of averaged saturation is well captured with the calculations. This reduction is out of the range of variation that was measured in laboratory experiments (compare figure 3-1). In general, a lowering of total suction might occur locally due to a separation of the bentonite and sand components by the preparation technique of the specimen or in situ by the assembly of the experiment. Clusters of sand might form, but this is only a very small scale effect. The overall osmotic suction of the buffer (i.e. the bentonite “grains”) is not influenced by the dry density of the buffer. In the following assessments the measured suction – water content relationship approximation provided by AECL will therefore be used.

The calculations with varying permeability values were also performed with the van Genuchten shape parameter value of 0.3 suggested by AECL. When the permeability is reduced to $4 \cdot 10^{-21}$ $m^2$ the measured and calculated times for full averaged saturation agree well. Compared to the measured permeability values for an effective clay density as in BCE and ITT (see figure 3-3) this value is at the lower end of the band. However, the evolution of averaged saturation is not captured with the calculations.

In order to keep the permeability value from the analytical solution and the measured suction – water content relationship as physical constraints a van Genuchten shape parameter of 0.04 will be used as basis in the calculations for the in-situ tests. Though the evolution of averaged saturation is not captured well for the water uptake test, the agreement is at least better than the fit by reducing only permeability, and also at least the time for full averaged water saturation is well captured for the water uptake test with this value.

It should be emphasized that this value for the shape parameter is not confirmed by available experimental results.

## 4.2 Buffer/Container Experiment and Isothermal Test

For the Isothermal Test and the Buffer/Container Experiment calculations were performed previously with two axially symmetric models (NOWAK 2008). These calculations had been revised for two reasons:

- The calibration with the water uptake test (compare previous chapter) was not yet completed.
- A new interface from GINA (BGR) to the 3-D mesh generation tool TetGen from the Weierstrass Institute for Applied Analysis and Stochastics (SI & GAERTNER 2005) had been developed and the parallelization of GeoSys/RockFlow had been enhanced. The BMs 2.1.1 and 2.1.2 offered an appropriate test case for field-scale application.

The governing equations are depicted in NOWAK (2007). Hydraulic processes are modelled with Richard's approximation (unsaturated flow); multiphase flow can be calculated with GS/RF, but not yet on parallel machines. Thermal processes are heat conduction and advection, whereas heat advection has no influence in the calculations presented in this report. Material behaviour is elastic with an additional term for swelling pressure $\mathbf{p}_{sw}$; this term has been modified recently as follows:

$$\mathbf{p}_{sw} = S_w p_{sw}^{max} \mathbf{I} \qquad (1)$$

In earlier versions swelling deformation was calculated proportional to the change of water saturation $S_w$ taken to the power of 2.

### 4.2.1 Finite Element Mesh

The geometry of the modelling domain was created as follows:

- digitalization of the ground view (including the shaft) of the 240 Level (compare figure 3-4, right hand side),
- extruding the digitized ground view in z-direction, modifying the width of the 240 Level excavations for a rounded contour,
- digital construction of ITT- and BCE-geometry with the given dimensions,
- and finally adding the geometry of outer boundaries for the modelling domain

The faces of the outer boundaries are aligned such that the measured primary stress field can be applied by loads and boundary conditions, see figure 4-6. For the results presented in this report this approach has no further influence. The approach has to be considered as case study for future calculations. The distance to the nearest excavations of 240 Level is several decameters.

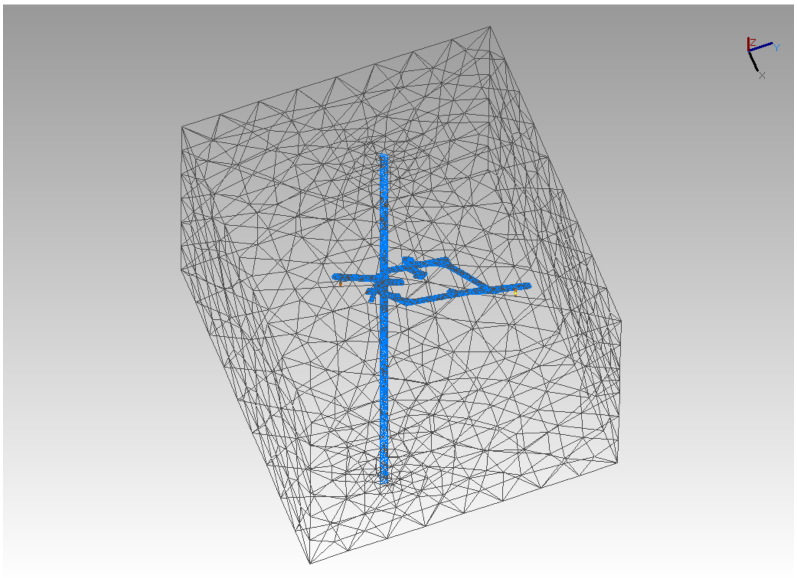

***Figure 4-6:*** *Mesh for BCE/ITT model.*

In total there are 77581 nodes in 483818 tetrahedral elements in this mesh. For the buffer in BCE 26736 nodes (125552 elements) are used and 4307 nodes (22848 elements) for the buffer in ITT, respectively. These numbers result from the geometry itself and following volume constraints:

- < 0.0003 $m^3$ for elements in ITT-buffer
- < 0.0002 $m^3$ for elements in BCE-buffer

Figure 4-7 shows in detail the mesh around BCE and ITT; the elements for the rock are blanked in this figure and only the outer surfaces of elements are shown. Sensor positions in the buffer are labelled.

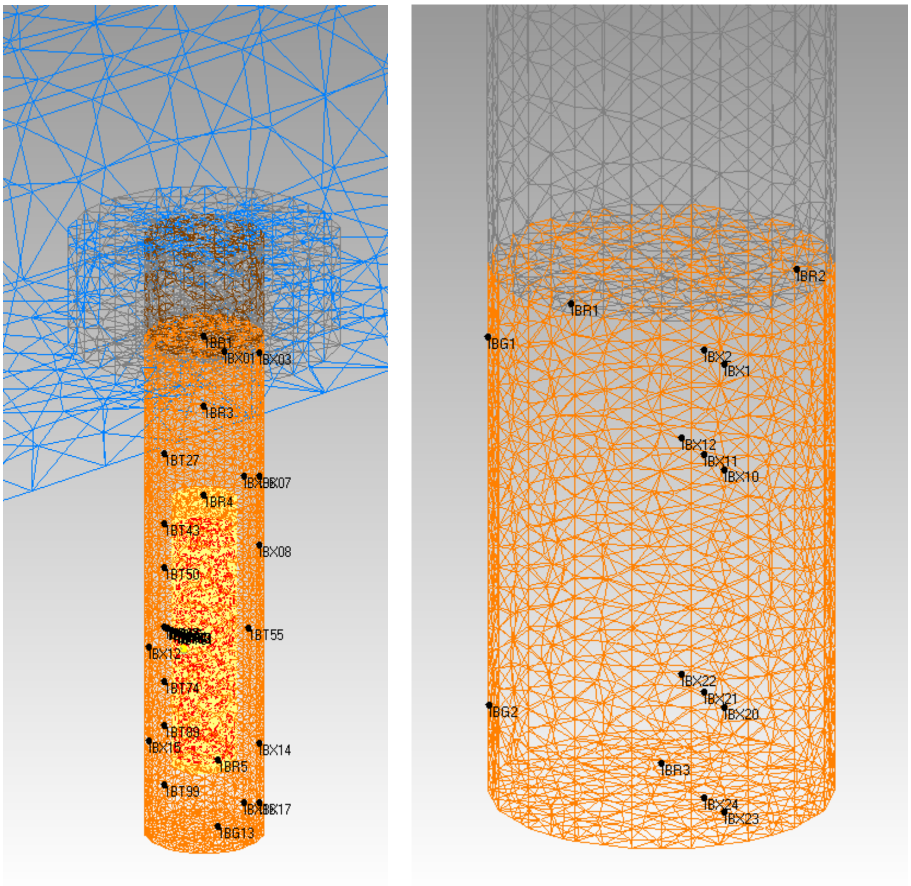

***Figure 4-7:*** *Detail BCE (left hand side) and ITT (right hand side) of the mesh.*

The automatic decomposition for parallel processing on 8 processors results in sub-domains ranging between 58906 and 62282 elements in size.

### 4.2.2 Initial and Boundary Conditions

Beneath the general capability of 3-D calculation a special interest was the modelling of excavation sequences. The influence on hydraulic processes was demonstrated in NOWAK (2008) using the example of time dependency of water influx into the ITT borehole.

The excavation of the 240 Level is roughly approximated by the following calculation sequence depicted in table 4-1:

**Table 4-1: Calculation sequence for BCE/ITT model.**

| time [d] | description (change of conditions) | steps |
|---|---|---|
| 0 - 366 | 240 m-level open (except room 205 and 213) | 13 |
| 366 - 456 | excavation of room 205 (ITT) | 3 |
| 456 - 562 | drilling of ITT-borehole | 4 |
| 562 - 896 | excavation of room 213 (BCE) | 12 |
| 896 - 1259 | drilling of BCE-borehole | 13 |
| 1259 - 1736 | installation of BCE | 164 |
| 1736 - 2355 | installation of ITT | 132 |
| 2355 - 4139 | dismantling of BCE (end: dismantling of ITT) | 171 |

Initially there is a hydrostatic pressure distribution in the entire modelling domain. Open excavation surfaces are put under a water pressure of -0.6 MPa (capillary pressure) which equals a water saturation of 0.82 for the rock. Outer boundaries are put under hydrostatic pressure as indicated in figure 4-8. The buffer in BCE has a water pressure of -4.45 MPa (suction) at installation which equals a water saturation of 0.88. The buffer in ITT has a water pressure of -4.9 MPa (suction) at installation which equals a water saturation of 0.84.

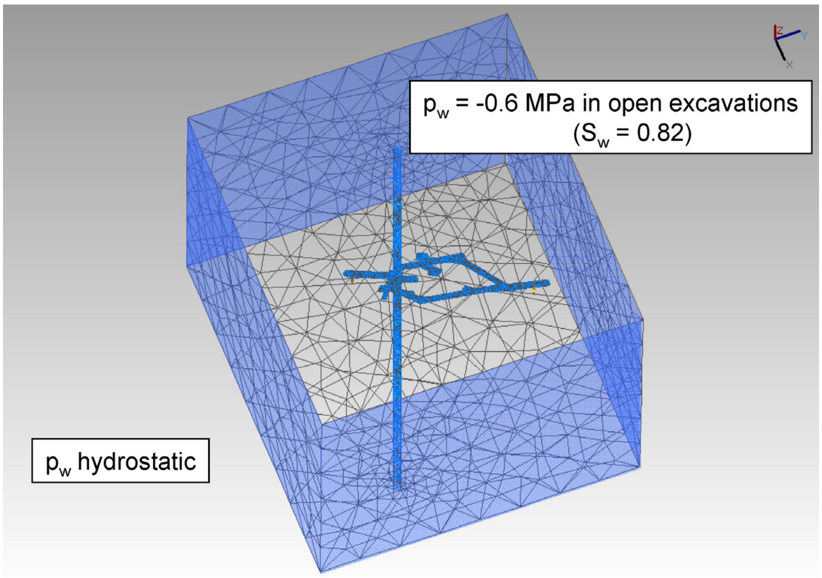

***Figure 4-8:*** *Hydraulic boundary conditions.*

Mechanical boundary conditions are summarized in figure 4-9. They represent the measured primary stress field and have to be considered as code testing for practical applications beyond the scope of BM 2.1.1 and 2.1.2.

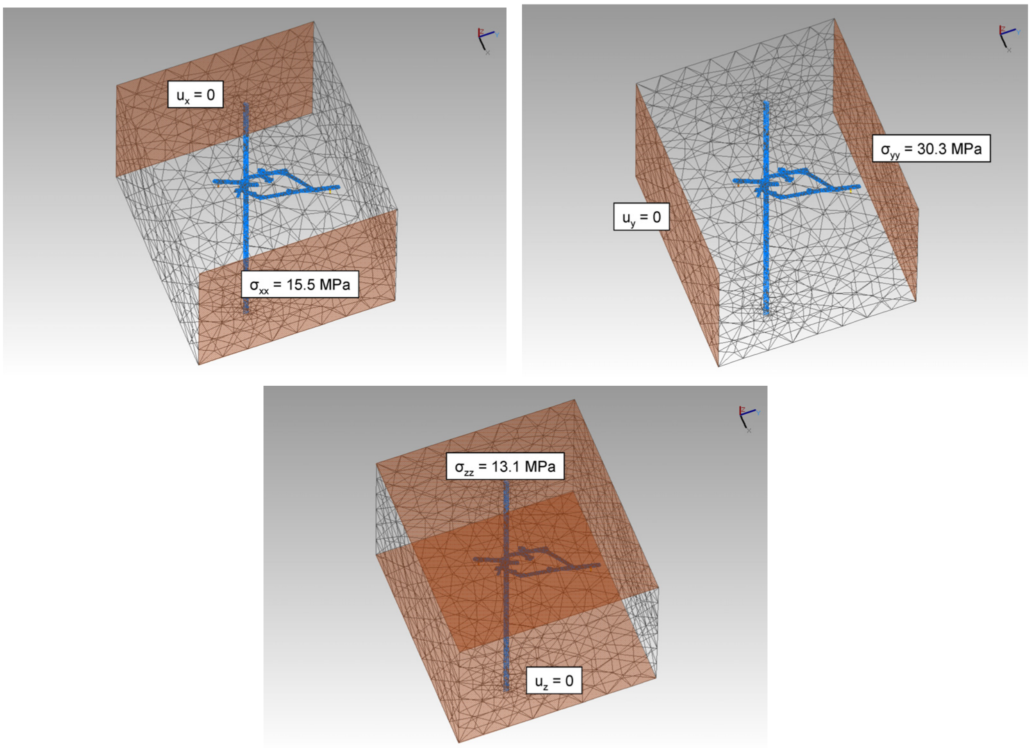

***Figure 4-9:*** *Mechanical boundary conditions.*

Initially there is a temperature of 12°C in the entire modelling domain. Thermal boundary conditions are 12°C at all outer boundaries. Measured temperatures at the container surface are averaged and set there also as boundary conditions.

### 4.2.3 Parameter Values

Heat capacity and heat conductivity of a porous medium are calculated according to the following equations which allow for the coupling of thermal and hydraulic properties:

$$c\rho = nS_w c_w \rho_w + n(1 - S_w)c_g \rho_g + (1 - n)c_s \rho_s \qquad (2)$$

$$\lambda = nS_w \lambda_w + n(1 - S_w)\lambda_g + (1 - n)\lambda_s \qquad (3)$$

with

$c$: heat capacity of porous medium or (with index) of phase (solid, gas, water)

$\lambda$: heat conductivity of porous medium or (with index) of phase

$\rho$: density of porous medium or (with index) of phase

$S$: phase saturation

$n$: porosity

Table 4-2 to 4-7 summarize the properties in the calculations.

**Table 4-2: Properties of the buffer.**

| parameter | value | source / status |
|---|---|---|
| (averaged) solid density $\rho_s$ [kg/m$^3$] | 2683 | calculated from $\rho_d$, $n$ in task description |
| porosity [-] | 0.359 | task description |
| permeability [m$^2$] | $5 \cdot 10^{-20}$ | analytically derived from water uptake test, see chapter 3.1.2 |
| van Genuchten $\beta$ [-] in eq. (2) | 0.04 | fitting value from water uptake test, see chapter 4.1.3 |
| gas entry pressure $P_0$ [MPa] in eq. (1) | 7 | WAN et al. (1995),<br>see also chapter 3.1.1 |
| shape par. $\beta_1$ [-] in eq.(1) | 0.73 | WAN et al. (1995),<br>see also chapter 3.1.1 |
| tortuosity [-] | 1 | not calibrated, influence on vapour diffusion, compare NOWAK (2007) |
| heat capacity $c_s$ [J/(kg*K)] | 1250 | fitting value |
| heat conductivity $\lambda_s$ [W/(m*K)] | 2 | fitting value |
| swell. pressure coeff. in eq. (3) [Pa] | $4 \cdot 10^6$ | fitting value,<br>compare introduction to chapter 4.2 |
| Young's modulus [Pa] | $2 \cdot 10^9$ | not calibrated,<br>compare introduction to chapter 4.2 |
| Poisson's ratio [-] | 0.44 | not calibrated,<br>compare introduction to chapter 4.2 |
| thermal expansion coefficient [K$^{-1}$] | $10^{-6}$ | NOWAK (2008) |

**Table 4-3: Properties of the backfill.**

| parameter | value | source / status |
|---|---|---|
| (averaged) solid density $\rho_s$ [kg/m$^3$] | 2696 | calculated from $\rho_d$, $n$ in task description |
| porosity [-] | 0.21 | task description |
| permeability [m$^2$] | $10^{-19}$ | not calibrated |
| van Genuchten $\beta$ [-] in eq. (2) | 0.04 | not calibrated (same as buffer) |
| gas entry pressure $P_0$ [MPa] in eq. (1) | 7 | not calibrated (same as buffer) |
| shape par. $\beta_1$ [-] in eq.(1) | 0.73 | not calibrated (same as buffer) |
| tortuosity [-] | 1 | not calibrated |
| heat capacity $c_s$ [J/(kg*K)] | 1055 | fitting value |
| heat conductivity $\lambda_s$ [W/(m*K)] | 1.5 | fitting value |
| swell. pressure coeff. in eq. (3) [Pa] | $1 \cdot 10^4$ | fitting value,<br>compare introduction to chapter 4.2 |
| Young's modulus [Pa] | $2 \cdot 10^9$ | not calibrated (same as buffer) |
| Poisson's ratio [-] | 0.44 | not calibrated (same as buffer) |
| thermal expansion coefficient [K$^{-1}$] | $1 \cdot 10^{-6}$ | not calibrated (same as buffer) |

**Table 4-4: Properties of the sand.**

| parameter | value | source / status |
|---|---|---|
| (averaged) solid density $\rho_s$ [kg/m$^3$] | 2650 | calculated from $\rho_d$, $n$ in task description |
| porosity [-] | 0.302 | task description |
| heat capacity $c_s$ [J/(kg*K)] | 757 | fitting value |
| heat conductivity $\lambda_s$ [W/(m*K)] | 0.4 | fitting value |
| Young's modulus [Pa] | $2 \cdot 10^9$ | not calibrated (same as buffer) |
| Poisson's ratio [-] | 0.4 | not calibrated (same as buffer) |
| thermal expansion coefficient [K$^{-1}$] | $1 \cdot 10^{-6}$ | not calibrated (same as buffer) |

**Table 4-5: Properties of the granite.**

| parameter | value | source / status |
|---|---|---|
| (averaged) solid density $\rho_s$ [kg/m$^3$] | 2643 | calculated from $\rho_d$, $n$ in task description |
| porosity [-] | 0.005 | task description |
| permeability [m$^2$] | $5 \cdot 10^{-20}$ | calibrated against water inflow measurements,<br>compare NOWAK (2008) |
| van Genuchten $\beta$ [-] in eq. (2) | 0.345 | AECL |
| gas entry pressure $P_0$ [MPa] in eq. (1) | 0.7 | AECL |
| shape par. $\beta_1$ [-] in eq.(1) | 0.33 | AECL |
| heat capacity $c_s$ [J/(kg*K)] | 1000 | fitting value |
| heat conductivity $\lambda_s$ [W/(m*K)] | 3 | fitting value |
| Young's modulus [Pa] | $7 \cdot 10^{10}$ | task description |
| Poisson's ratio [-] | 0.3 | task description |
| thermal expansion coefficient [K$^{-1}$] | $3.8 \cdot 10^{-6}$ | task description |

**Table 4-6: Properties of the material group for the open excavations.**

| parameter | value | source / status |
|---|---|---|
| density $\rho_s$ [kg/m$^3$] | 1.19 | same as air |
| porosity [-] | 1 | open excavation |
| heat capacity $c_s$ [J/(kg*K)] | 1007 | same as air |
| heat conductivity $\lambda_s$ [W/(m*K)] | 0.026 | same as air |

**Table 4-7: Properties of the concrete.**

| parameter | value | source / status |
|---|---|---|
| (averaged) solid density $\rho_s$ [kg/m$^3$] | 2643 | assumption (same as granite) |
| porosity [-] | 0.21 | assumption (same as backfill) |
| permeability [m$^2$] | $10^{-19}$ | assumption, not calibrated |
| van Genuchten $\beta$ [-] in eq. (2) | 0.345 | assumption (same as granite) |
| gas entry pressure $P_0$ [MPa] in eq. (1) | 0.7 | assumption (same as granite) |
| shape par. $\beta_1$ [-] in eq.(1) | 0.33 | assumption (same as granite) |
| heat capacity $c_s$ [J/(kg*K)] | 1000 | assumption (same as granite) |
| heat conductivity $\lambda_s$ [W/(m*K)] | 3 | assumption (same as granite) |
| Young's modulus [Pa] | $7 \cdot 10^{10}$ | assumption (same as granite) |
| Poisson's ratio [-] | 0.3 | assumption (same as granite) |
| thermal expansion coefficient [K$^{-1}$] | $3.8 \cdot 10^{-6}$ | assumption (same as granite) |

With respect to heat conductivity eq. (3) equals 1.5 for the buffer, 1.3 for the backfill, and 0.46 for the sand in saturated state. In the case of unsaturated flow heat capacity and conductivity of the gas phase are taken as zero. Heat capacity and conductivity of the liquid phase are taken as 4200 J/(kgK) and 0.6 W/(mK), respectively; density of the liquid phase is modelled with 1000 kg/m$^3$ (compressible). Values for heat capacity and conductivity of the porous media in the in-situ experiments are available in the task description for some of the materials. Heat conductivity and capacity of the solid phase was adjusted to fit the measured temperatures in buffer and rock.

Relative permeability for water and intrinsic permeability of the buffer were calibrated against the water uptake test, compare chapter 4.1. The permeability of the granite was calibrated against the water influx into ITT- and BCE-borehole with the previous axially symmetric models, compare NOWAK (2008). Further hydraulic properties were taken from the task description or assigned reasonable assumed values in case they were considered to be insignificant for the requested results (backfill, concrete, sand).

### 4.2.4 Temperatures in BCE

Figure 4-10 shows the vertical temperature profile along the axis of BCE from the lid to the bottom of the buffer at four times (BCE output no. 1a). For orientation the areas are shaded as follows: red for heater, yellow for sand, orange for buffer, and grey for rock, compare figure 4-7. The profile for day 0 is not plotted, because it would be just a straight line along 12 °C according to the initial conditions. Measured values are from sensor 1BT17 and 1BT100 at bottom of buffer.

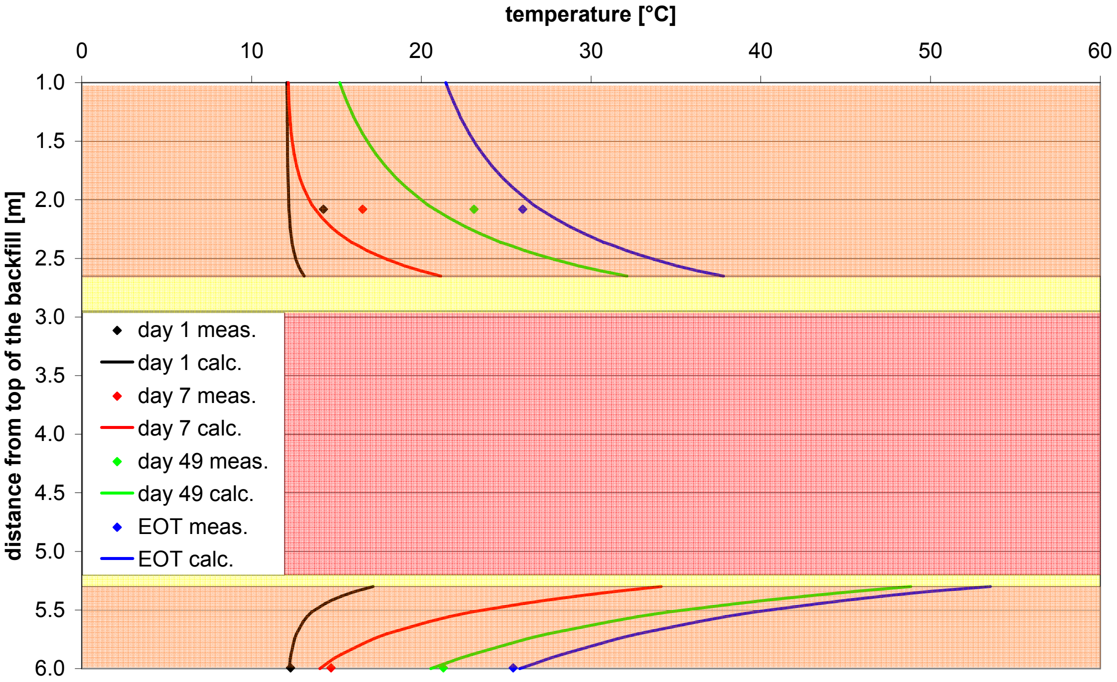

***Figure 4-10:*** *Temperature profile vertically along BCE axis from lid to bottom of buffer (BCE output 1a).*

Figure 4-11 shows the temperature profile radially outwards from the heater at mid-height into the surrounding rock at four times (BCE output no. 1b). Measured values in the buffer are from sensors 1BT61-67, measured values in the rock are from 1RM53, 1RM61, 1RM69, 1RM77, and 1RM85. Colour shading is as described for the previous figure.

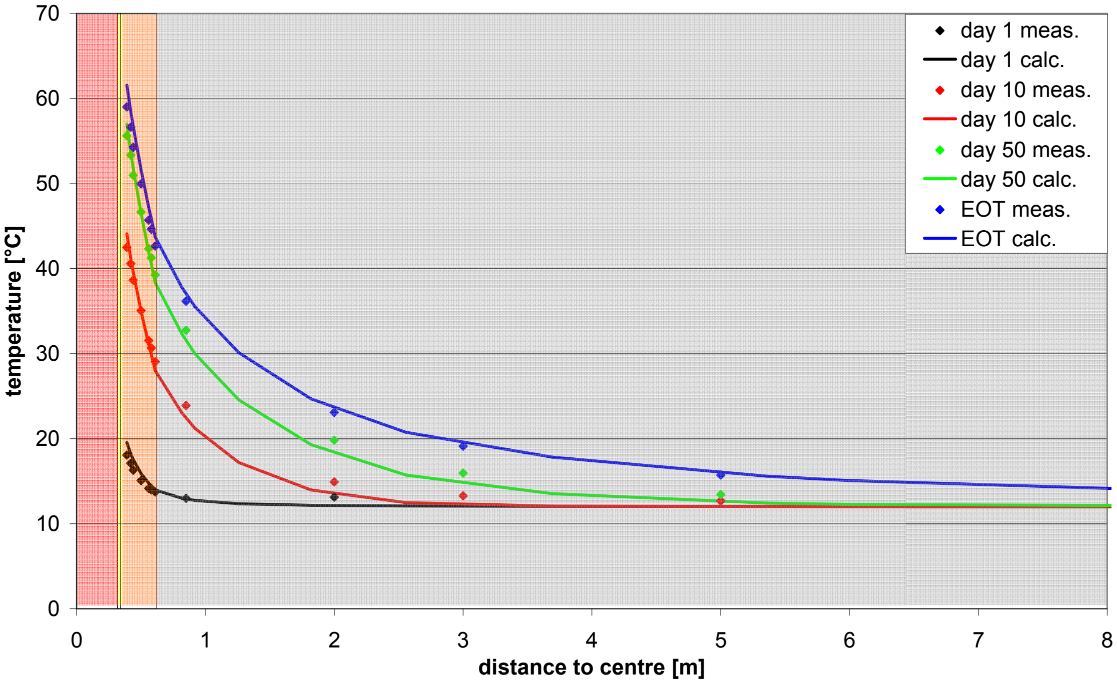

***Figure 4-11:*** *Temperature profile radially outwards from heater at mid-height into the surrounding rock (BCE output 1b).*

Figure 4-12 shows additionally the temperature evolution at sensors 1BT61-67.

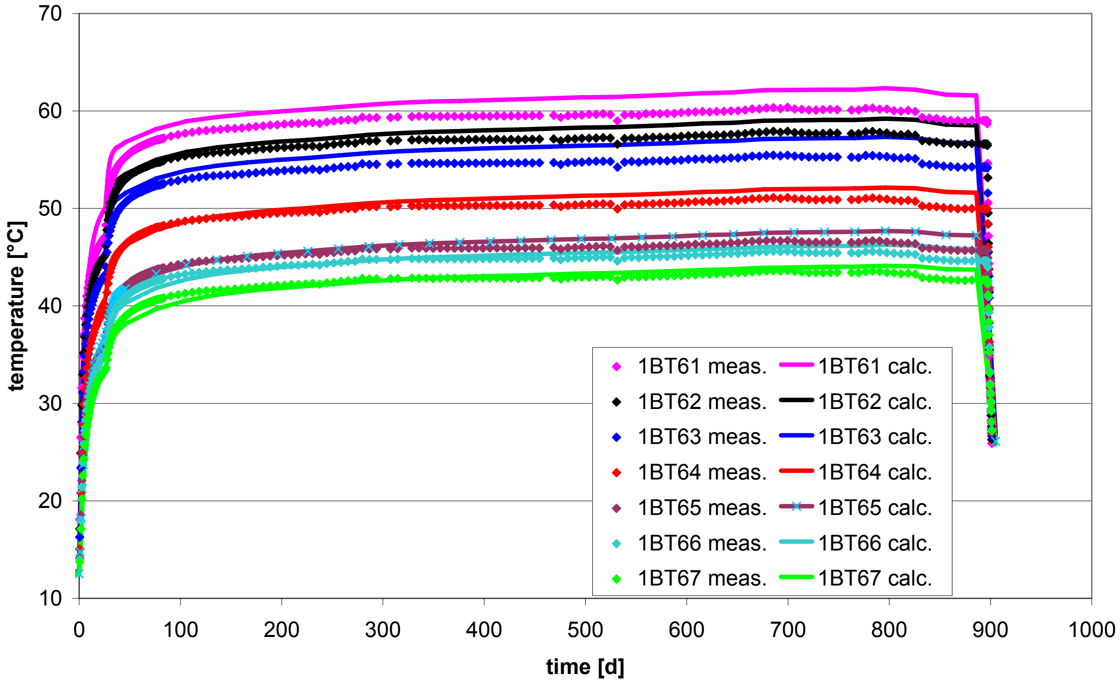

***Figure 4-12:*** *Temperature evolution at sensors 1BT61-67 in the buffer at heater mid-height.*

Figure 4-13 shows the temperature distribution in the buffer in section CC (BCE output no. 1c).

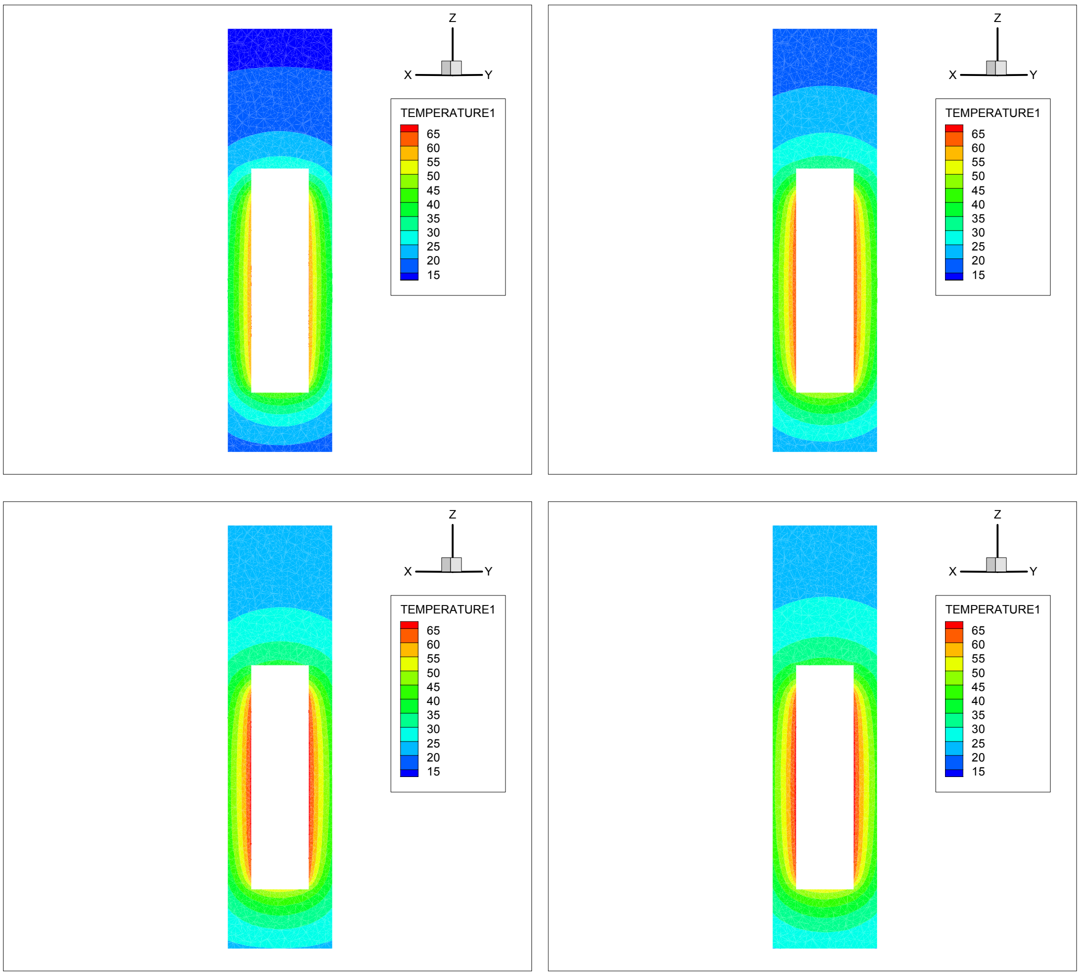

***Figure 4-13:*** *Temperature distribution in section CC: 30d, 136d, 406d, and at end of test (BCE output 1c).*

Figure 4-14 shows the temperature distribution in the surrounding rock in a section transverse to room 213 through the emplacement borehole, figure 4-15 in a section longitudinal to room 213 through the emplacement borehole at four times (BCE output no. 1d). Colour legend ranges between 14°C (blue) and 42°C (red).

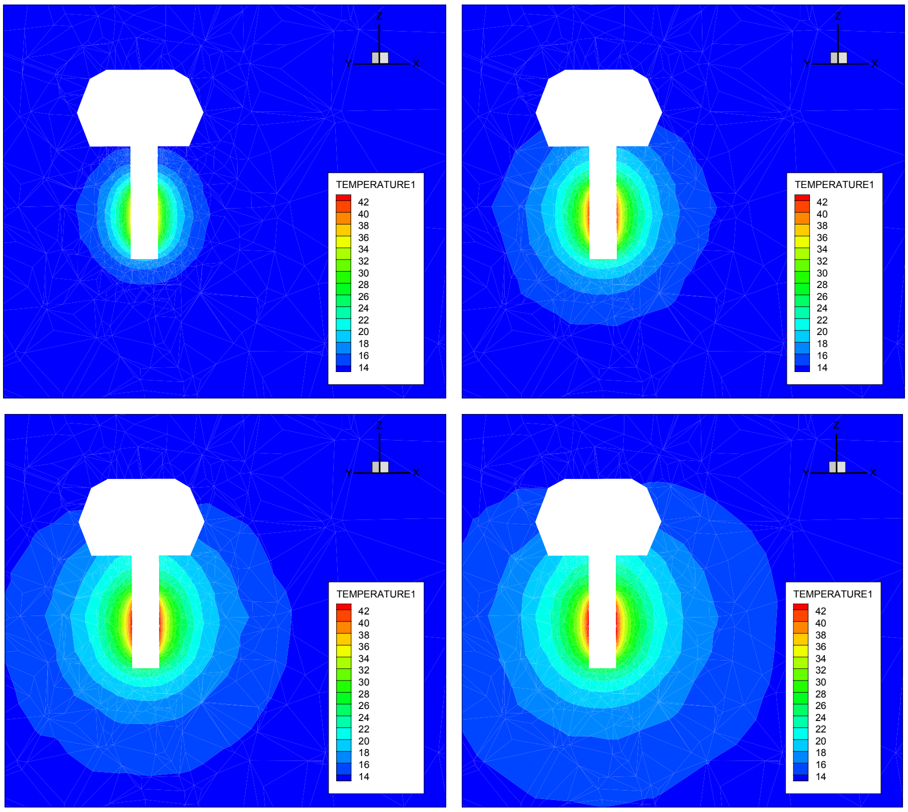

***Figure 4-14:*** *Temperature distribution in transverse section: 30d, 136d, 406d, and at end of test (BCE output 1d).*

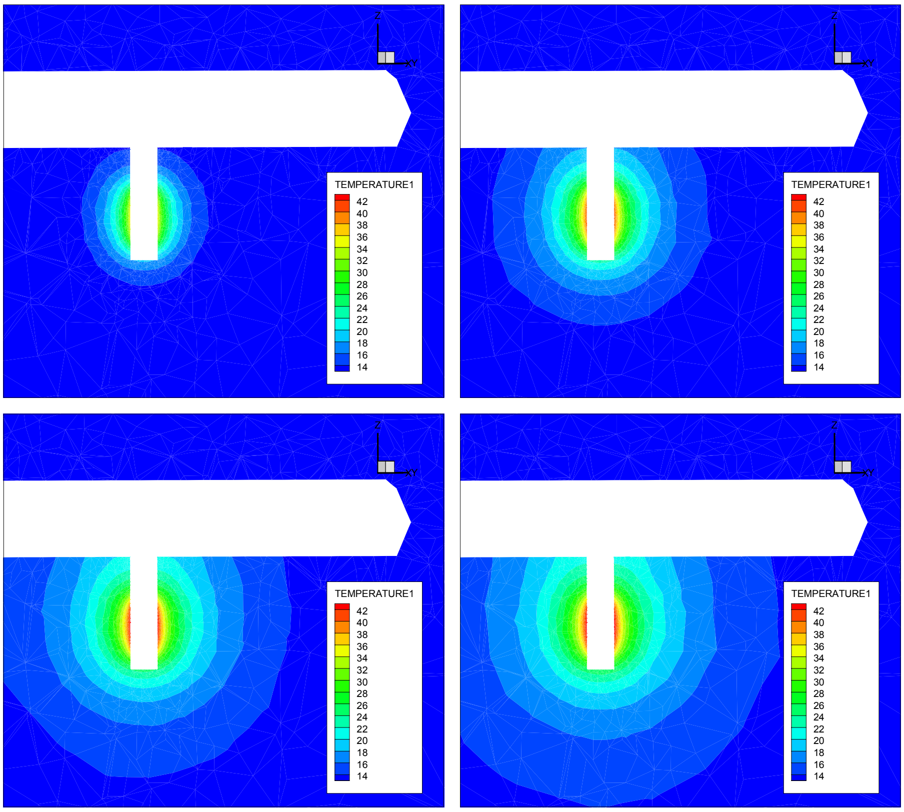

***Figure 4-15:*** *Temperature distribution in longitudinal section 30d, 136d, 406d, and at end of test (BCE output 1d.)*

For orientation figure 4-16 shows the location of the temperature sensors in the boreholes T7 and T8.

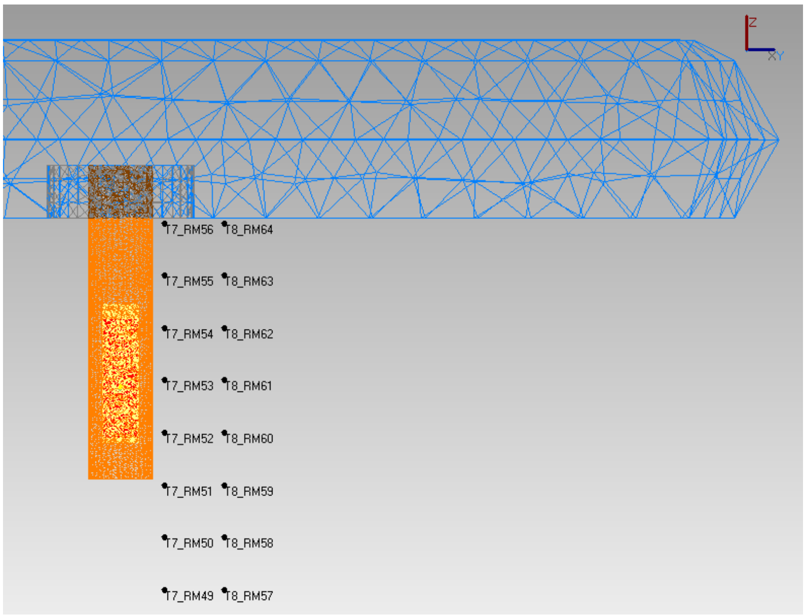

***Figure 4-16:*** *Sensor locations in boreholes T7 and T8.*

Figure 4-17 shows the temperature profile vertically along borehole T7 at four times (BCE output no. 1e). The profile for day 0 is not plotted, because it would be just a straight line along 12 °C according to the initial conditions. Measured values are from sensors 1RM49-56.

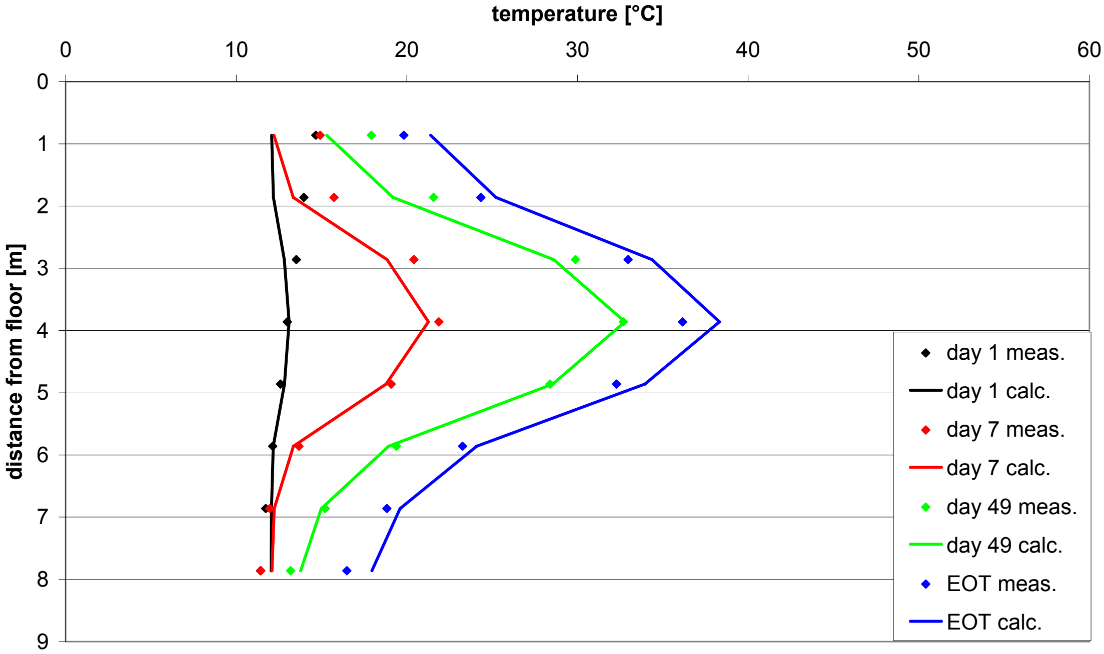

***Figure 4-17:*** *Temperature profile vertically along borehole T7 (BCE output 1e).*

Figure 4-18 shows the temperature profile vertically along borehole T8 at four times (BCE output no. 1e). The profile for day 0 is not plotted, because it would be just a straight line along 12 °C according to the initial conditions. Measured values are from sensors 1RM57-64.

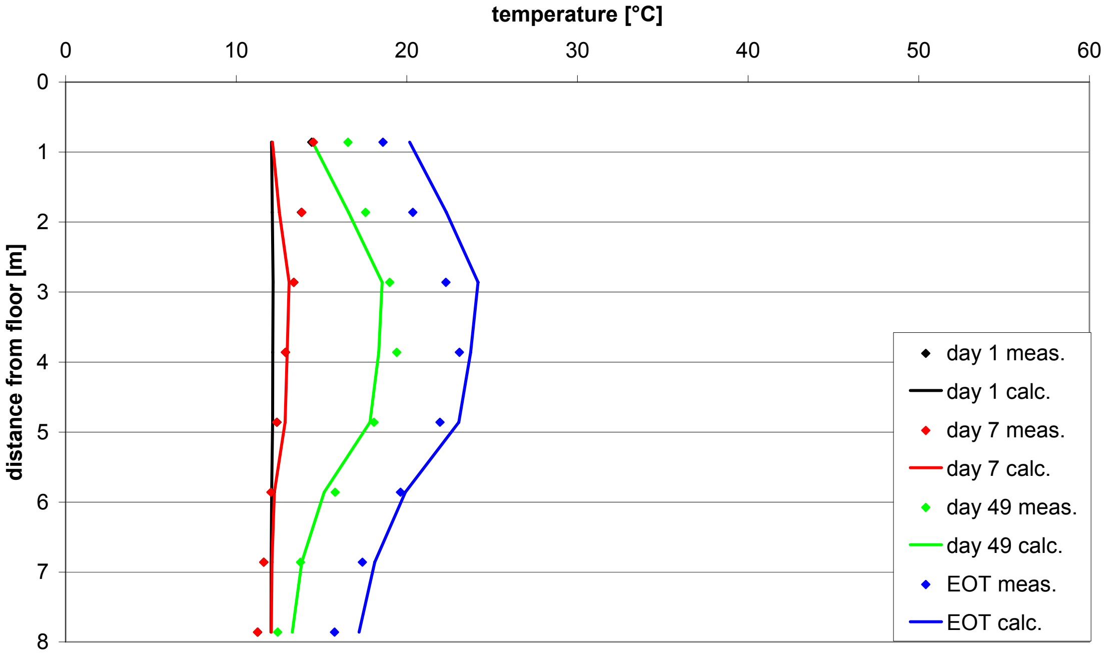

***Figure 4-18:*** *Temperature profile vertically along borehole T8 (BCE output 1e).*

Figure 4-19 shows additionally the temperature evolution at the sensors in borehole T7.

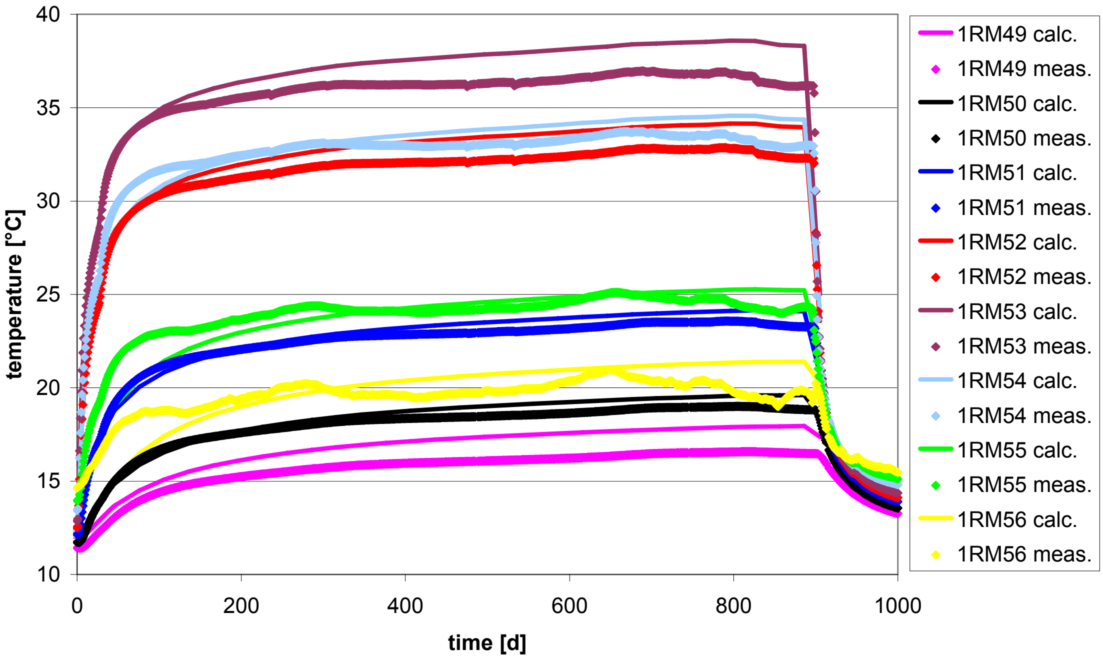

***Figure 4-19:*** *Temperature evolution at sensors in borehole T7.*

Figure 4-20 shows additionally the temperature evolution at the sensors in borehole T8.

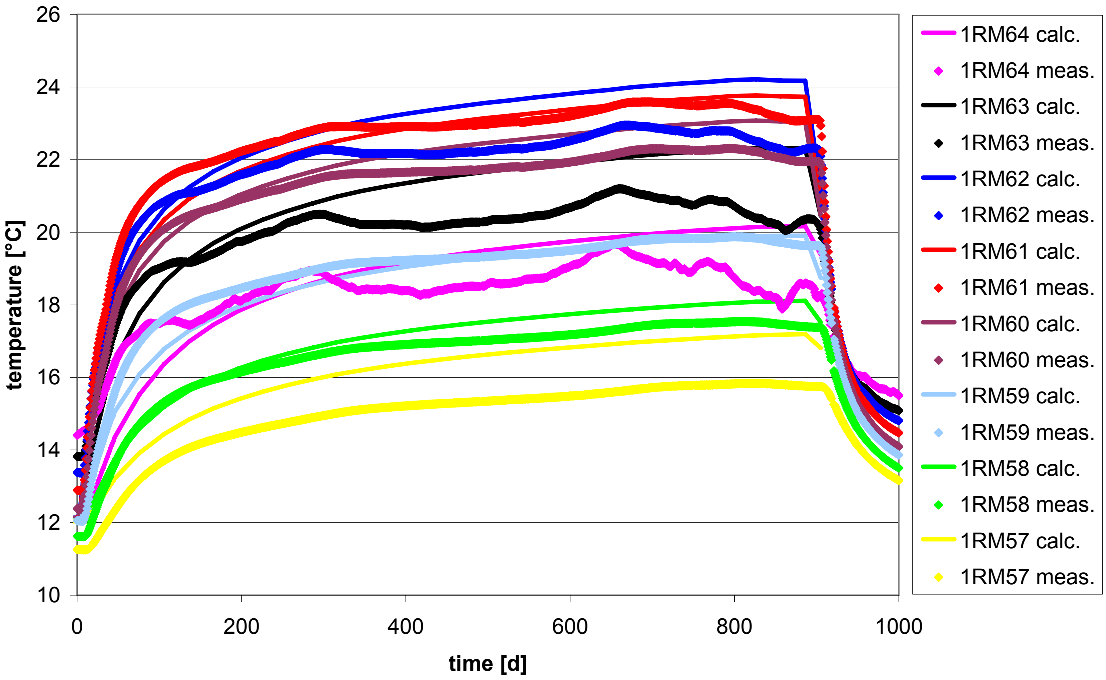

***Figure 4-20:*** *Temperature evolution at sensors in borehole T8.*

### 4.2.5 Water Pressure in the Rock around BCE

For orientation figure 4-21 shows the location of the axial and transversal profile lines for water pressure.

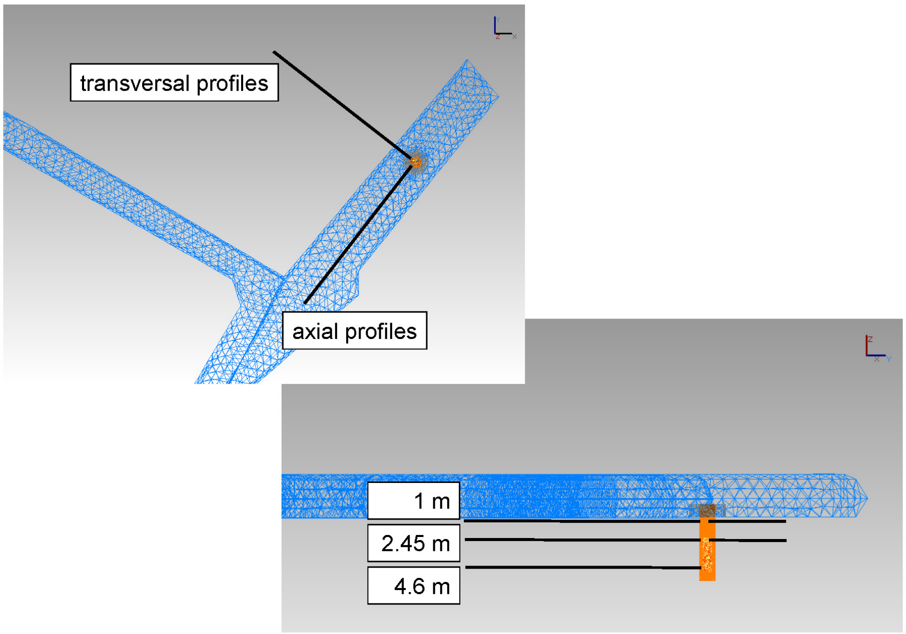

***Figure 4-21:*** *Location of axial and transversal profiles.*

Figure 4-22 shows the water pressure profile along room 213 (filled symbols for measured values with sensors 1RW7, 1RW12, and 1RW16, continuous lines for calculated values) and transversal to room 213 (open symbols for measured values with sensors 1RW20 and 1RW22, dashed lines for calculated values) 1 m below floor (BCE output no. 2a).

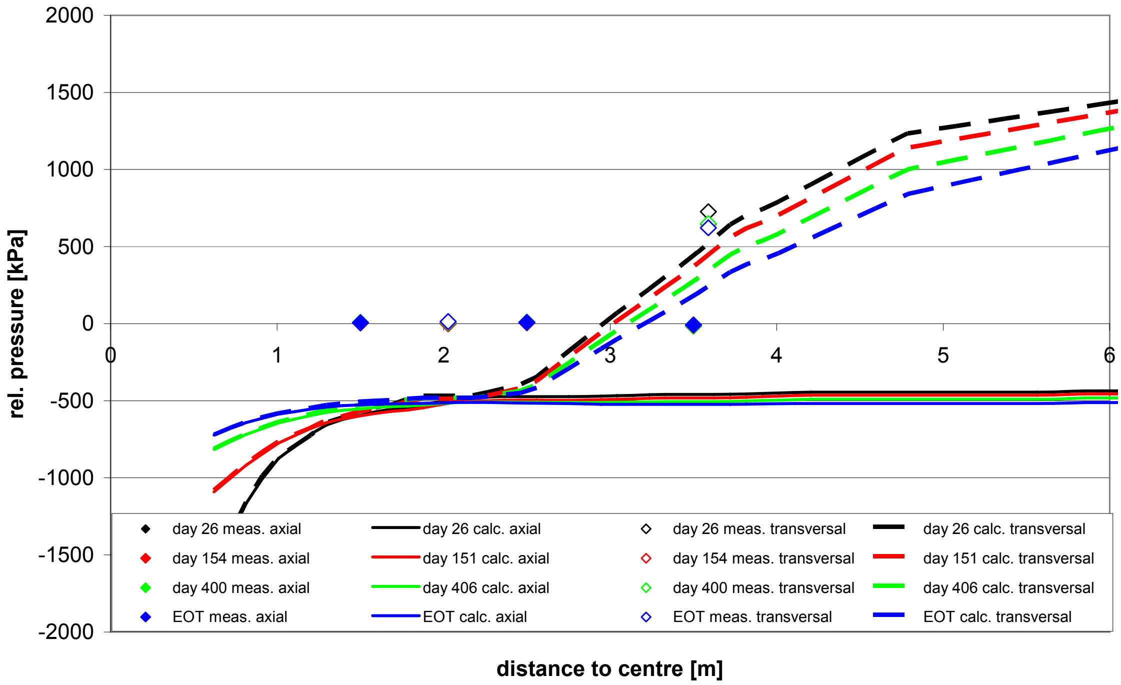

***Figure 4-22:*** *Water pressure distribution 1 m from the floor of room 213 (BCE output 2a).*

Figure 4-23 shows the water pressure profile along room 213 (filled symbols for measured values with sensors 1RW8, 1RW13, and 1RW17, continuous lines for calculated values) and transversal to room 213 (open symbols for measured values with sensors 1RW21 and 1RW23, dashed lines for calculated values) 2.45 m below floor (BCE output no. 2a).

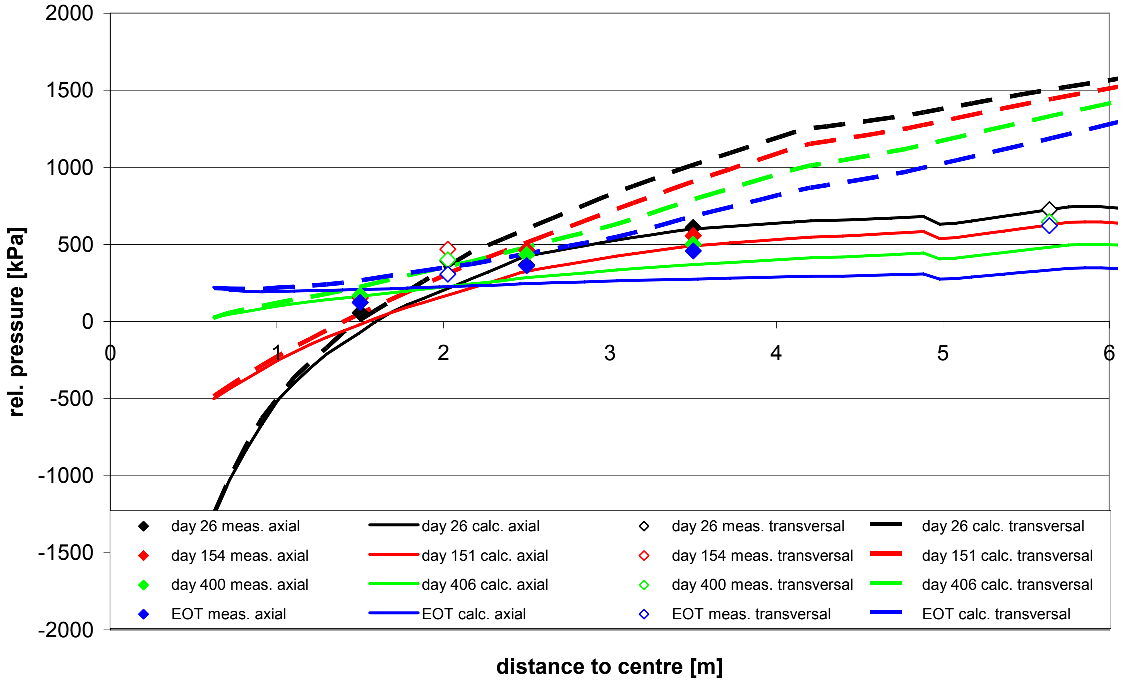

***Figure 4-23:*** *Water pressure distribution 2.45 m from the floor of room 213 (BCE output 2a).*

Figure 4-24 shows the water pressure profile along room 213 (filled symbols for measured values with sensors 1RW9, 1RW14, and 1RW18, continuous lines for calculated values) 4.6 m below floor (BCE output no. 2a).

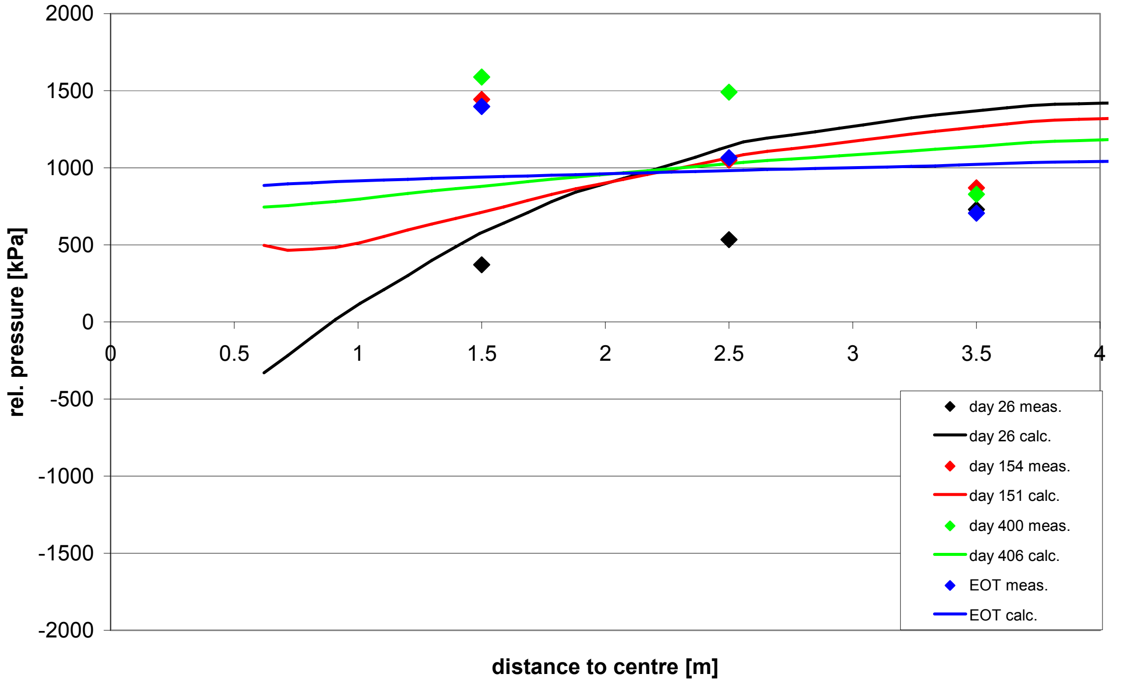

***Figure 4-24:*** *Water pressure distribution 4.6 m from the floor of room 213 (BCE output 2a).*

Figure 4-25 shows the water pressure evolution at sensors IRH1 to IRH4 which are located in the immediate vicinity of the emplacement borehole (BCE output no. 2b).

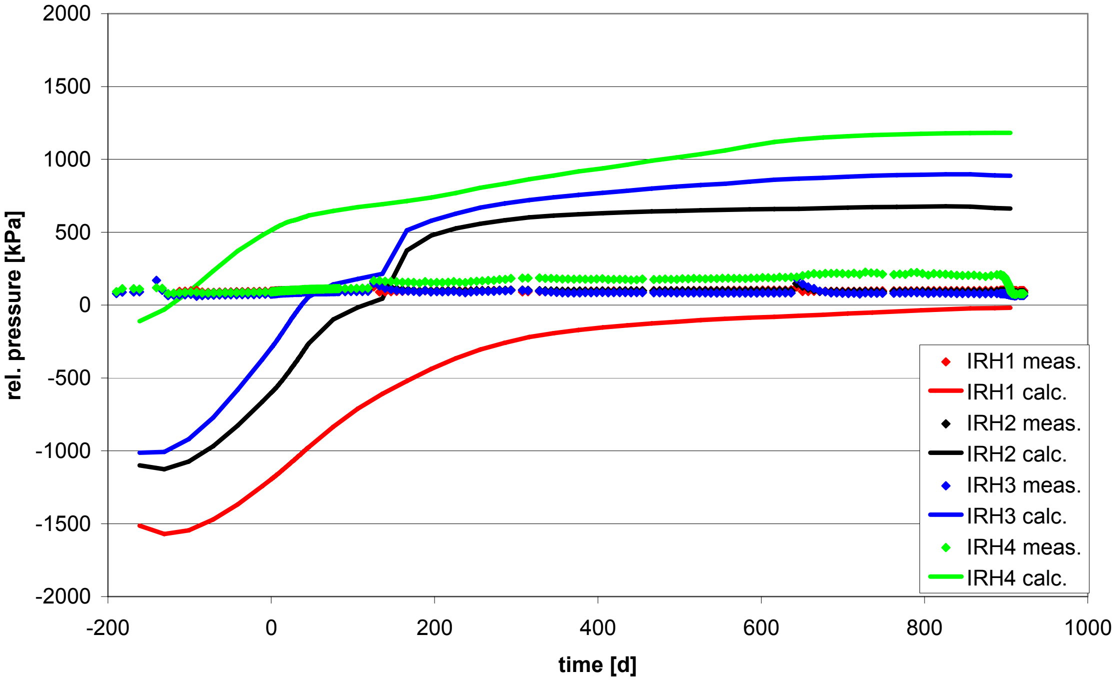

***Figure 4-25:*** *Water pressure evolution in sensors IRH1 to IRH4 (BCE output 2b).*

The measured water pressures in the boreholes HG9 (1.5 m from BCE axis), HG7 (3.5 m from BCE axis), and HG10 (5.64 m from BCE axis) show a clear reaction to the thermal pulse from the heater. This reaction is plotted in the following figures as pressure derivatives with black symbols. The calculated pressure derivatives (plotted with red symbols) do not show this reaction. The change rate of maximum principal stress is plotted with blue symbols. These diagrams are discussed in chapter 5.

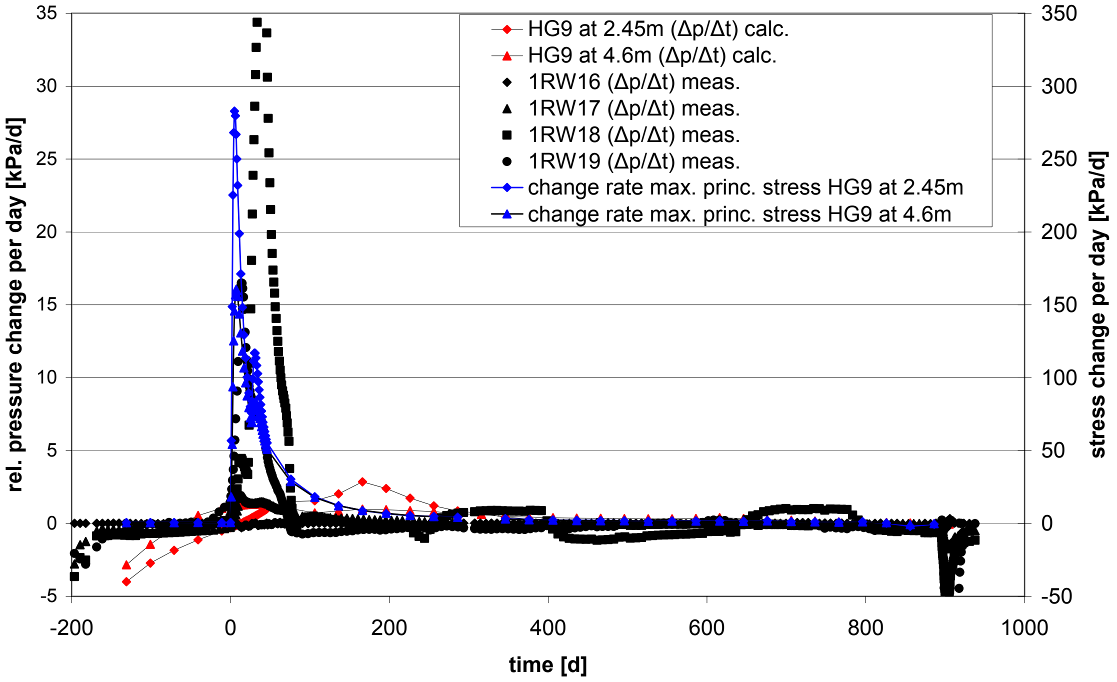

*Figure 4-26: Pressure and stress derivatives for borehole HG9.*

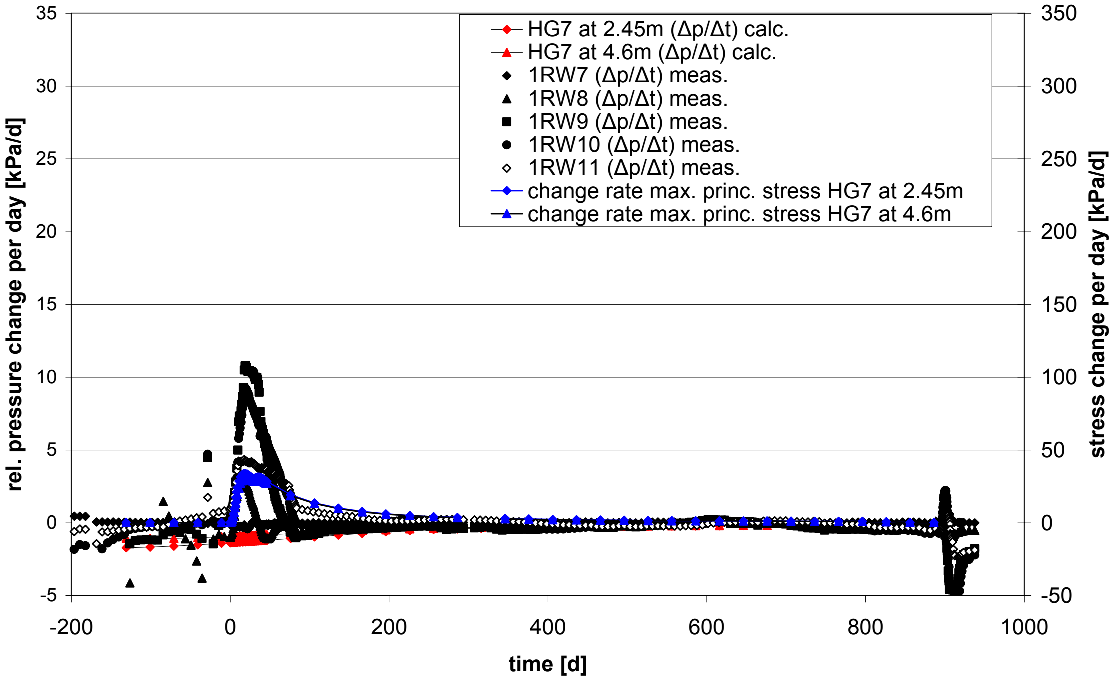

*Figure 4-27: Pressure and stress derivatives for borehole HG7.*

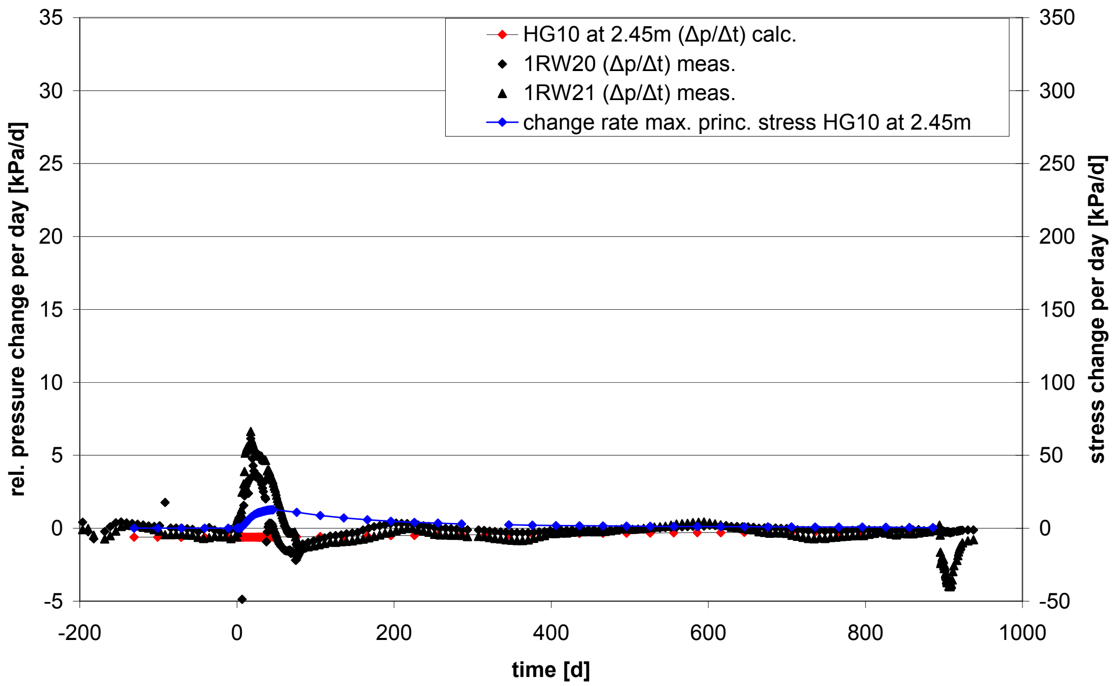

*Figure 4-28: Pressure and stress derivatives for borehole HG10.*

### 4.2.6 Water Pressure in the Rock around ITT

For orientation figure 4-29 depicts the sensor positions for water pressure measurements in the rock around ITT.

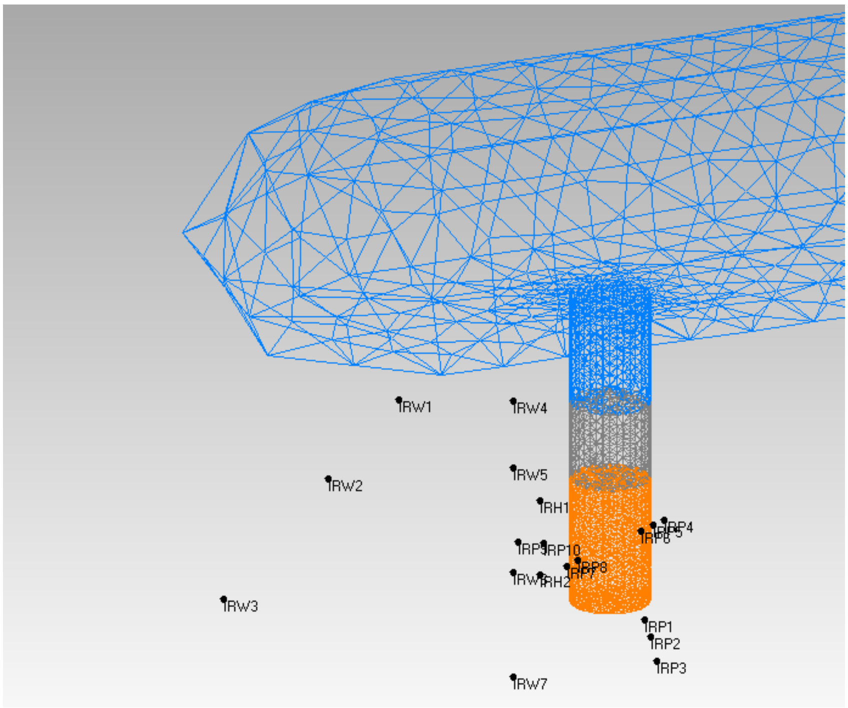

*Figure 4-29: Sensor positions in the rock around ITT.*

Figure 4-30 shows the water pressure evolution at sensors IRP2 to IRP4 which are located in the vicinity of the emplacement borehole (ITT output no. 1b).

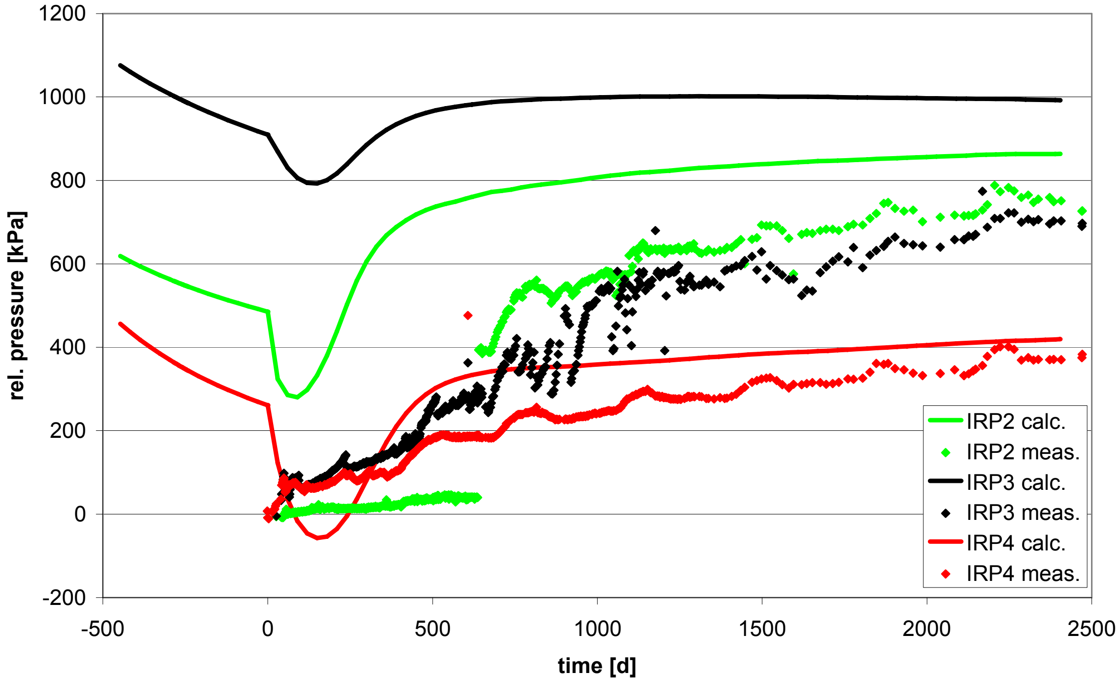

***Figure 4-30:*** *Water pressure evolution in sensors IRP2 to IRP4 (ITT output 1b).*

Figure 4-31 shows the water pressure profile at buffer mid-height (filled symbols for measured values with sensors IRH2, IRW6, and IRW3, continuous lines for calculated values) (ITT output no. 1c).

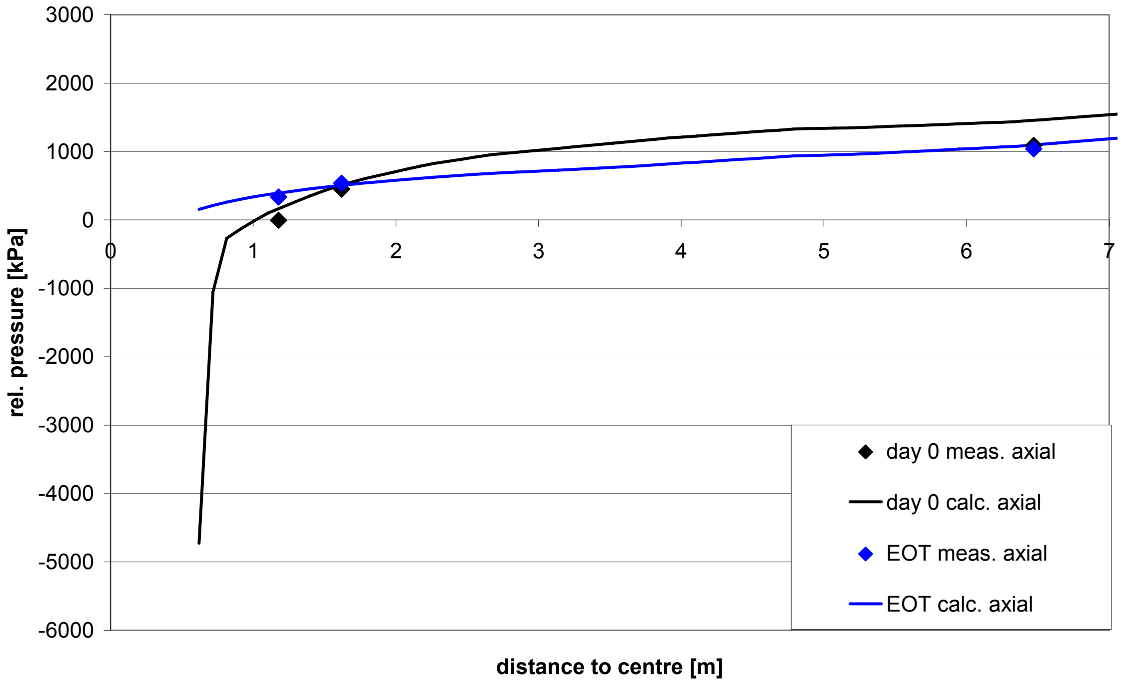

***Figure 4-31:*** *Water pressure distribution at buffer mid-height (ITT output 1c).*

### 4.2.7 Water Content in the Buffer of BCE

Figure 4-32 shows the water content distribution in the buffer in a vertical cross section through the buffer at end of test (BCE output no. 3a). The plot was prepared as scatter plot (nodes coloured according to the water content).

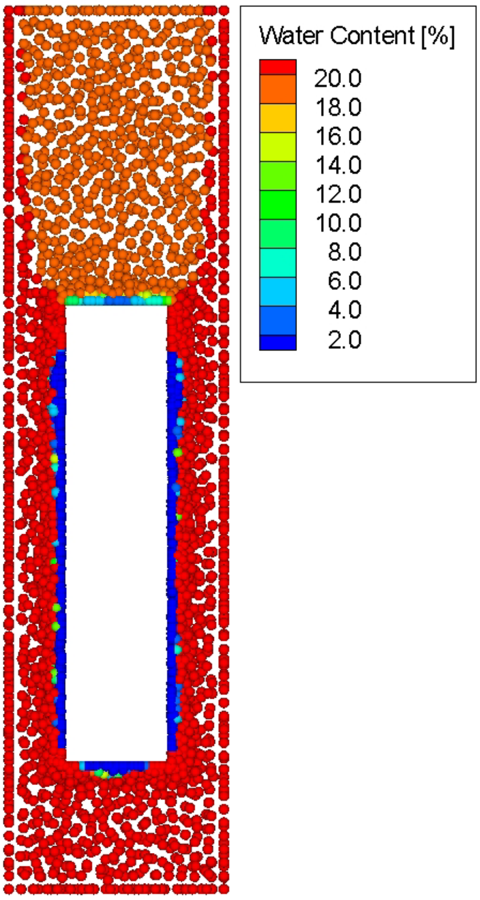

***Figure 4-32:*** *Water content distribution in vertical cross section through the buffer at end of test (BCE output 3a.)*

Figure 4-33 shows the water content evolution at several sensors (BCE output no. 3b). The theoretical maximum of water content is 20.9% (compare chapter 3.1.1).

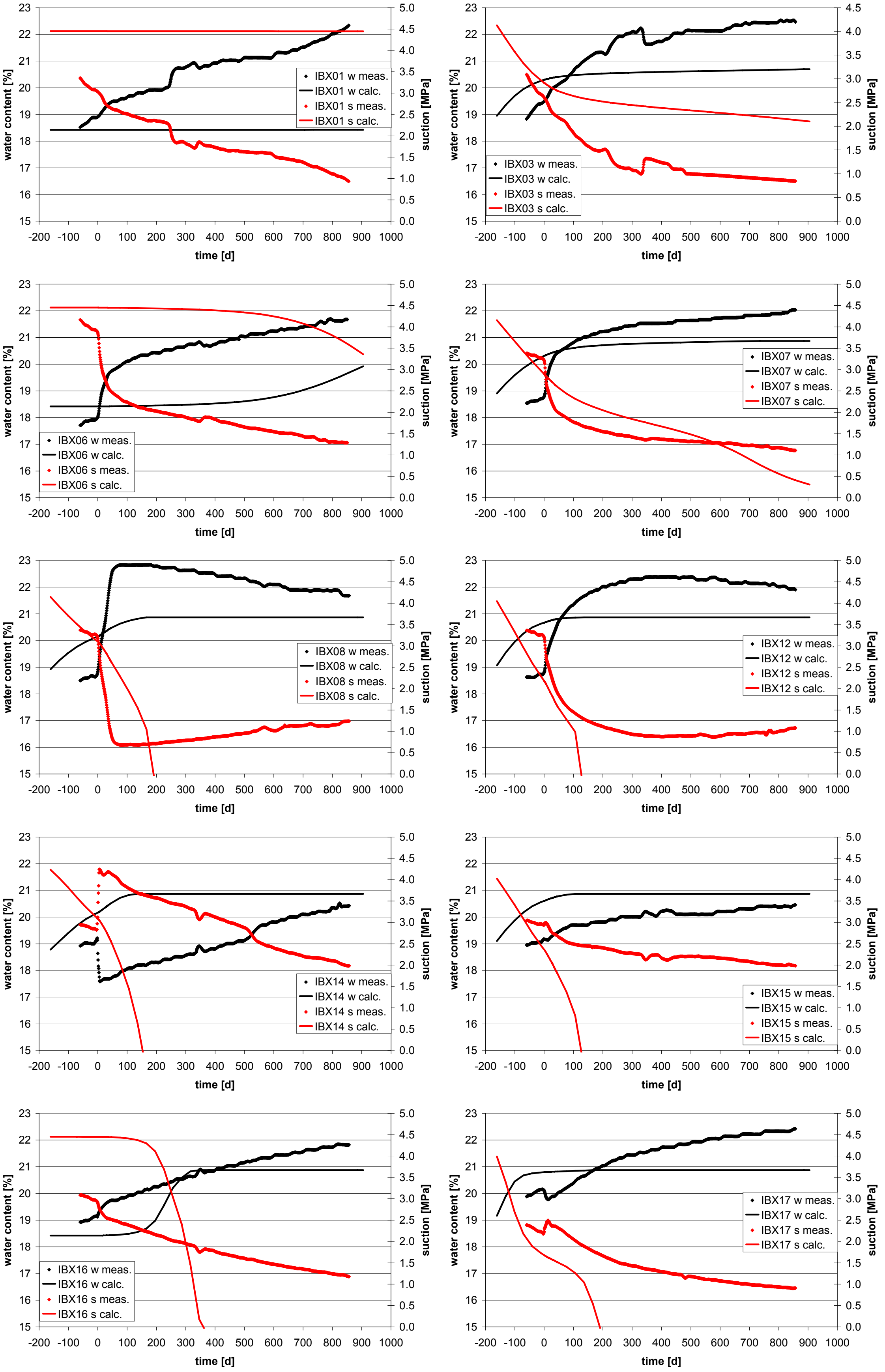

***Figure 4-33:** Water content evolution at several sensors in BCE (BCE output 3b).*

### 4.2.8 Water Content in the Buffer of ITT

Figure 4-34 shows the water content profile at elevations 0.5 m, buffer's mid-height (1.0 m), and 1.5 m radially outwards from the borehole centreline at several points in time (ITT output no. 2a). The bottom of the borehole is zero elevation.

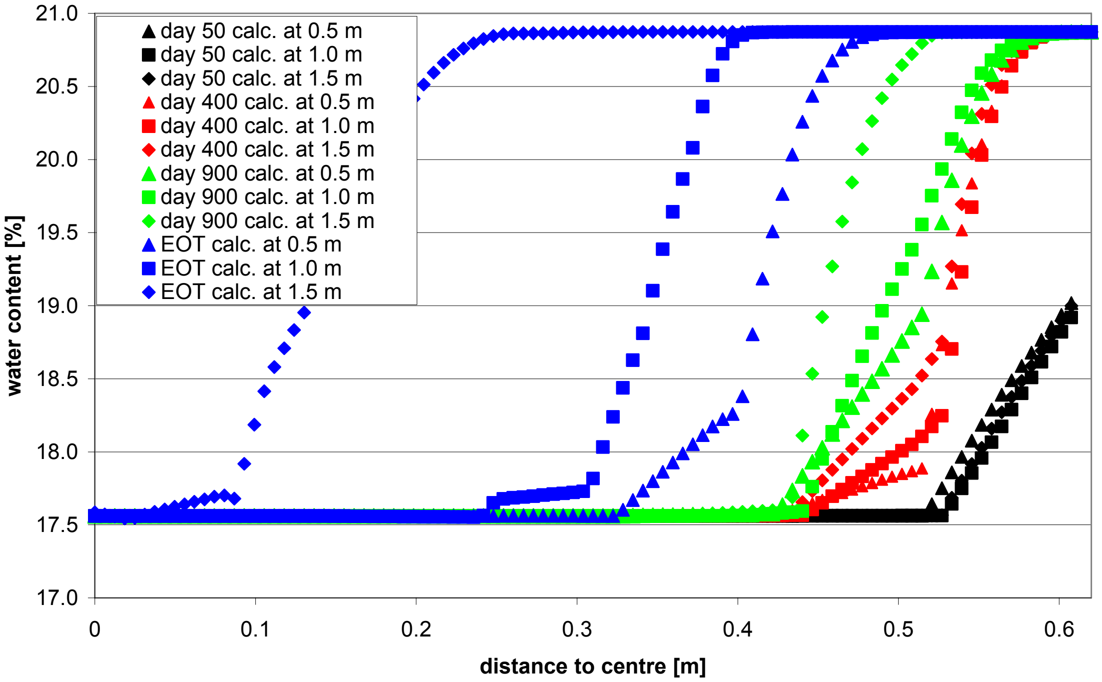

***Figure 4-34:*** *Water content profile at several times and elevations (ITT output 2a).*

Figure 4-35 shows the water content distribution at 50 d, 400 d, 900 d, and 1500 d in a vertical cross section through ITT (ITT output no. 2b). The plot was prepared as scatter plot (nodes coloured according to the water content).

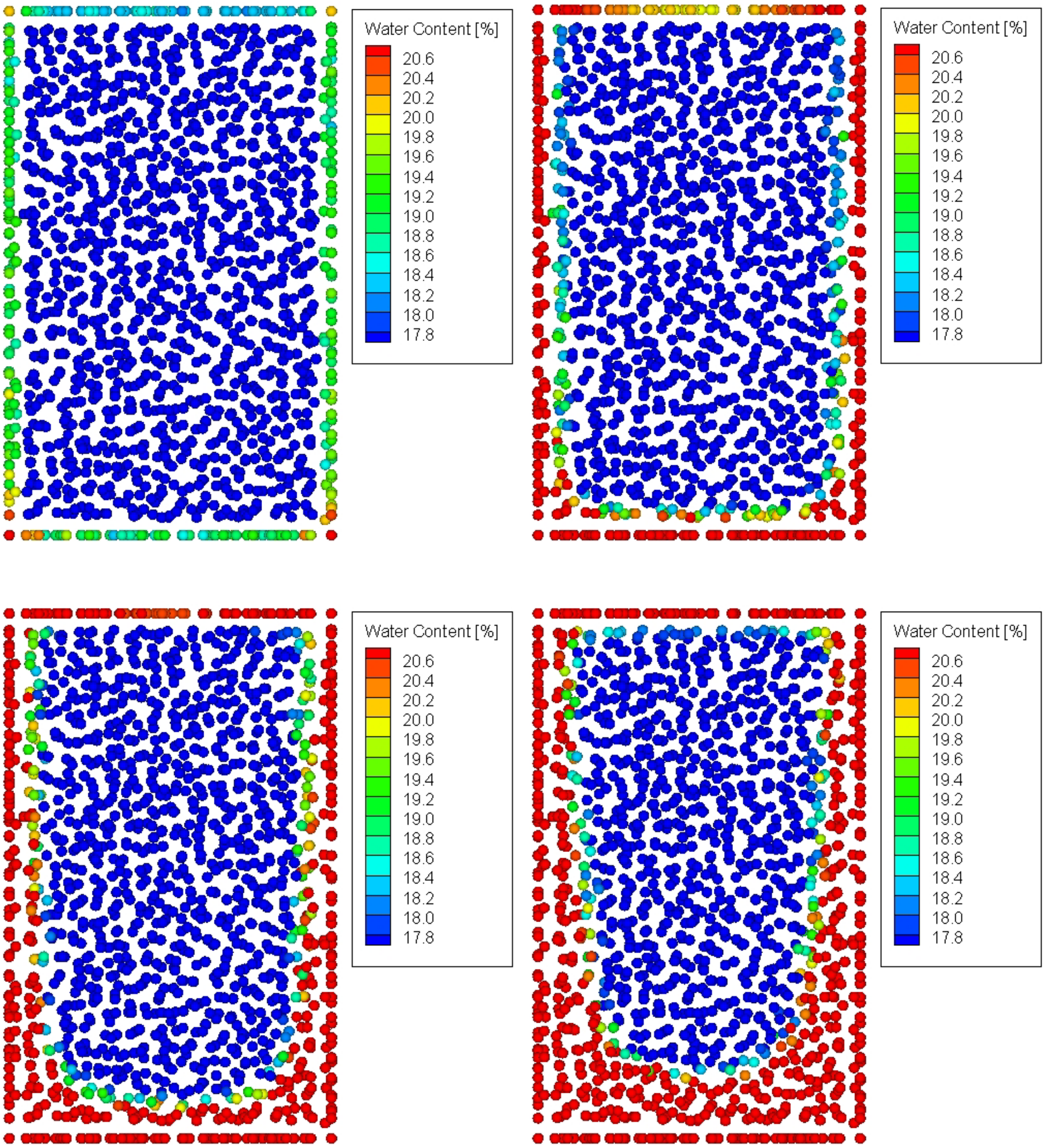

***Figure 4-35:*** *Water content distribution at 50d, 400d, 900d, and 1500d in vertical cross section (ITT output 2b).*

Figure 4-36 shows the water content profile at layer A to H radially outwards from the borehole centreline at the end of test (ITT output no. 2c).

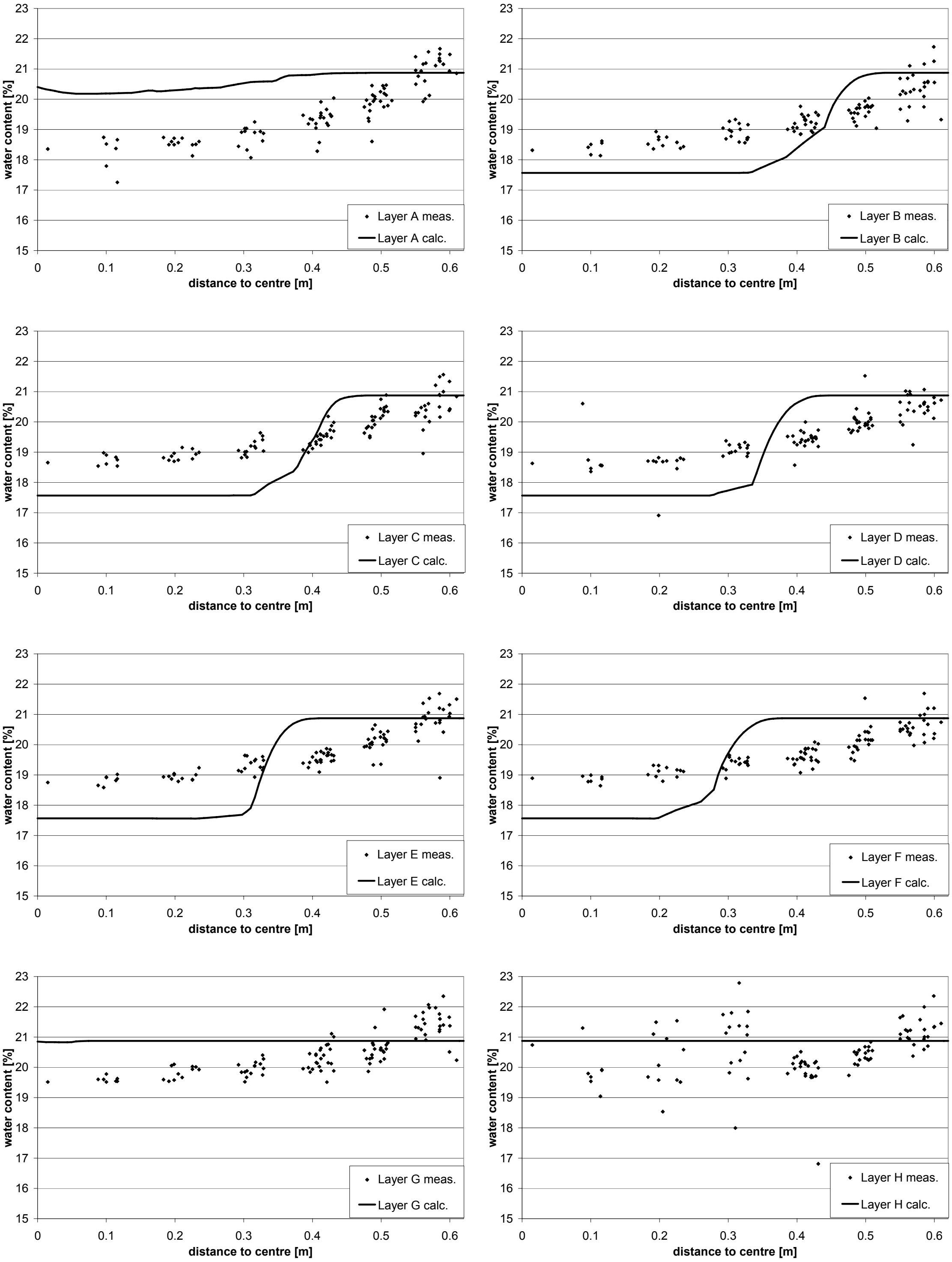

***Figure 4-36:*** *Water content profile in layers A to H at end of test (ITT output 2c).*

Figure 4-37 shows additionally the water content evolution at several sensors of ITT. The theoretical maximum of water content is 20.9% (compare chapter 3.1.1).

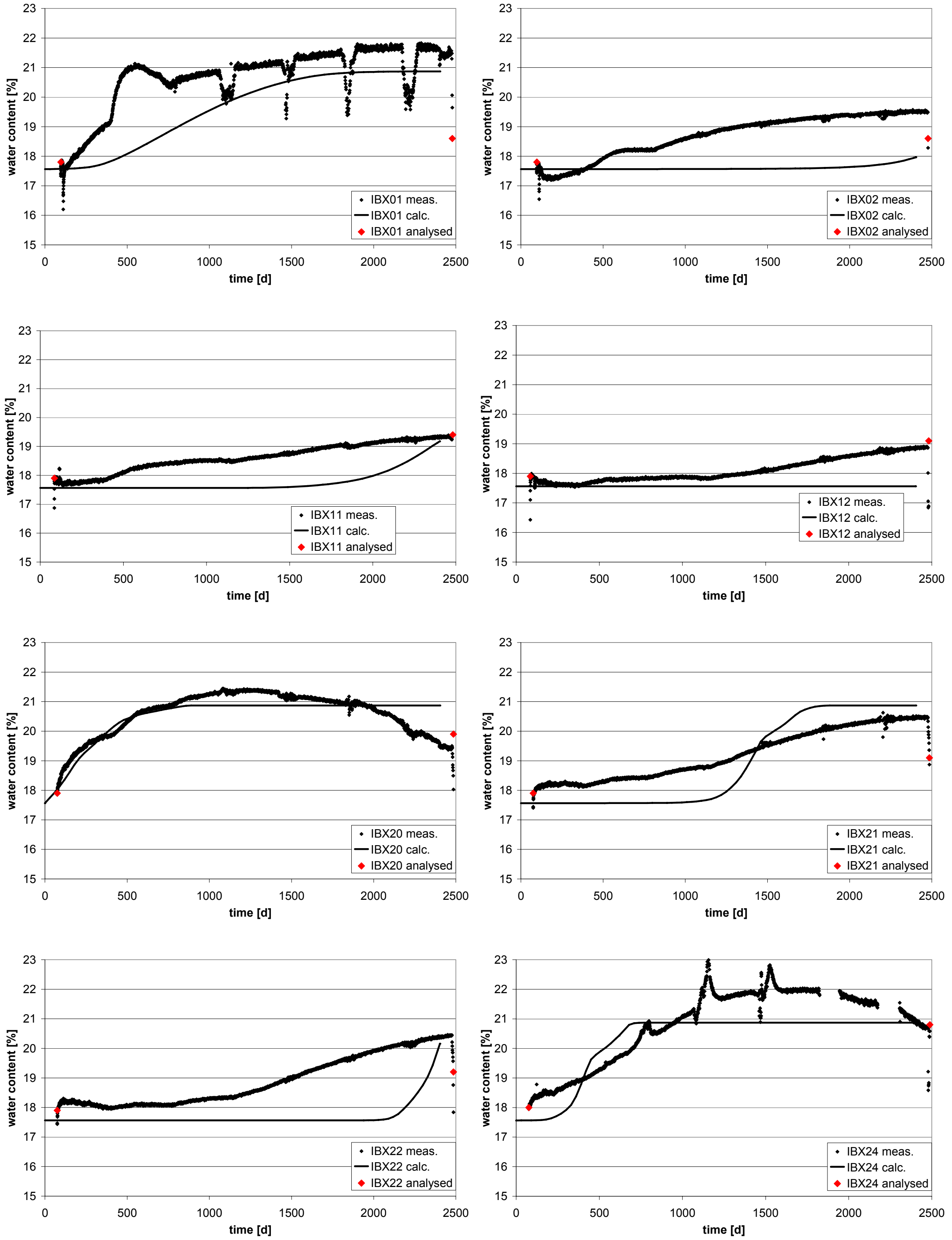

***Figure 4-37:*** *Water content evolution at several sensors in ITT.*

### 4.2.9 Total Pressure in the Buffer of BCE

Figure 4-38 shows the measured evolution of total pressure in comparison to the calculated change of maximum principle stress at sensors 1BR1, 1BR3 to 5, and 1BR13 (BCE output no. 4a). The calculated data is shifted such that measured and calculated value at day 0 is equal.

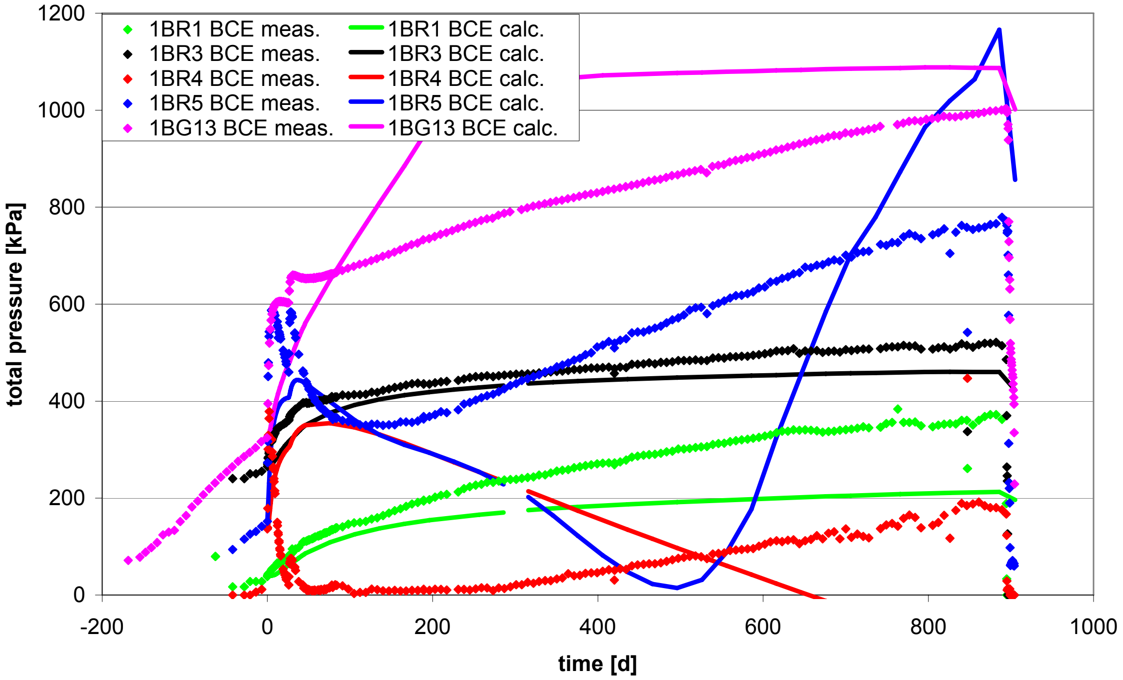

***Figure 4-38:*** *Measured total pressure evolution and calculated change of maximum principle stress in sensors 1BR1, 1BR3 to 1BR5, and 1BG13 (BCE output 4a).*

### 4.2.10 Total Pressure in the Buffer of ITT

Figure 4-39 shows the measured evolution of total pressure in comparison to the calculated change of maximum principle stress at sensors IBR1 to 3 (ITT output no. 3a). The calculated data is shifted such that measured and calculated value at day 0 is equal.

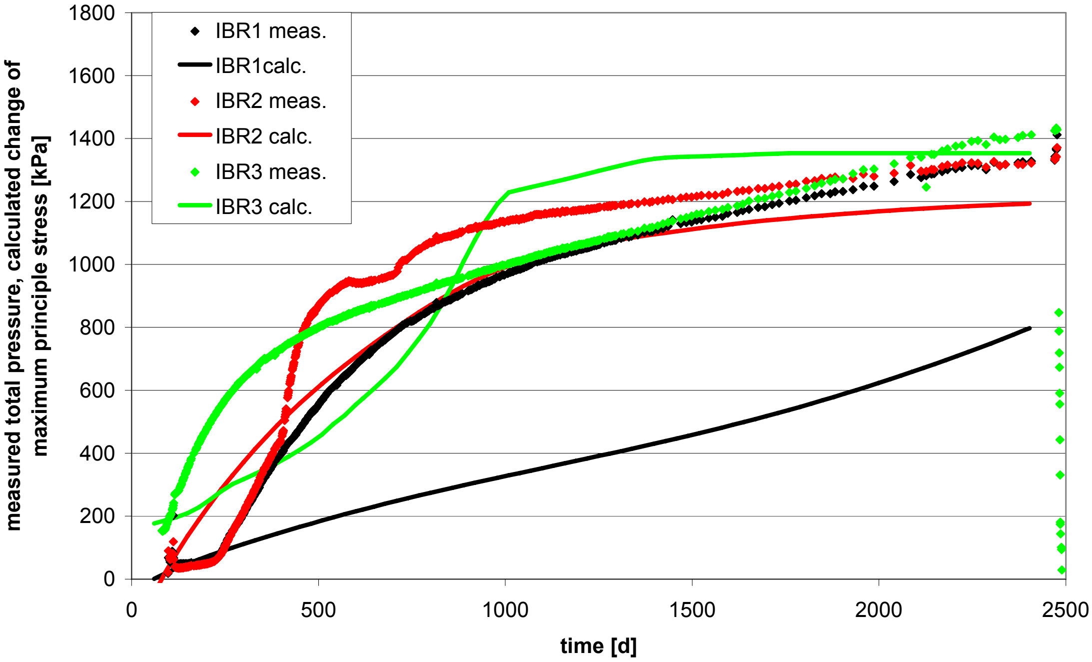

***Figure 4-39:*** *Measured total pressure evolution and calculated change of maximum principle stress in sensors IBR1 to IBR3 (ITT output 3a).*

Figure 4-40 shows the measured evolution of total pressure in comparison to the calculated change of maximum principle stress at sensors IBG1 and IBG2 (ITT output no. 3b). The calculated data is shifted such that measured and calculated value at day 0 is equal.

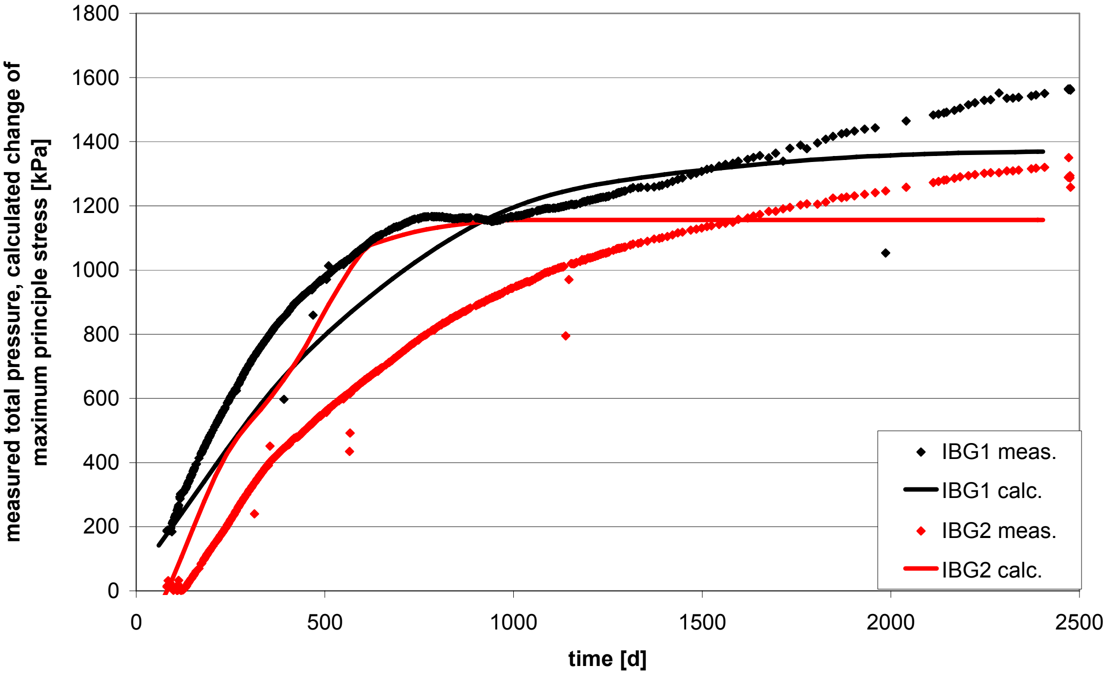

***Figure 4-40:*** *Measured total pressure evolution and calculated change of maximum principle stress in sensors IBG1 and IBG2 (ITT output 3b).*

The requested outputs for total pressure evolutions radially outwards (requested output no. 4b) and the vertical displacement profiles along the EXT boreholes (requested output no. 4c) were not processed.

# 5 Discussion

With respect to temperature the calculated values agree over all very well with the measured data, see for example the profile radially outwards from heater into the rock in figure 4-11.

The temperature profile vertically along BCE axis (figure 4-10) shows a nearly perfect agreement with the measured values from sensor 1BT100 at the bottom of the buffer. For the sensor 1BT17 in the upper buffer section the calculated temperature value is between 1 and 2°C below the measured value for day 1, 7, and 49. From the measured data (for example for borehole T7) it can be easily recognized that there had been some heater testing prior to the main heating phase. This heater testing and in general the weathering of the URL might have caused an initial temperature distribution different to the modelled 12°C in the entire modelling domain. At the end of the test the calculated value for 1BT17 is slightly higher than the measured value. This can be explained by the heat advection due to the weathering of room 213 which is not taken into account in the model. This effect can also be recognized in the deviation between calculated values and measured data in the boreholes T7 (figure 4-17) and T8 (figure 4-18).

The measured water pressure in the rock around BCE in a distance of 1 m below the floor (figure 4-22) shows zero (relative) pressure in axial direction (filled symbols) throughout the complete duration of the test. This observation indicates that the rock is unsaturated in that area. If the rock had been saturated the water filled test intervals would have reacted on any temperature increase. The calculated values for the axial direction (continuous lines) coincide with the measured data in the sense that the rock is unsaturated; this is due to the (fitted, but reasonable) boundary condition of -0.6 MPa suction on open excavation surfaces (compare figure 4-8). With this boundary condition the measured (positive) pressures transversal to room 213 (open symbols) are met by the calculated values in a distance of about 3.5 m from the BCE axis.

For the depth of 2.45 m from the floor of room 213 (figure 4-23) the majority of the calculated values still agree well with the measured data or they show the correct tendency with evolving time (decreasing pressure at a distance of 3.5 m from BCE axis, increasing pressure at a distance of 1.5 m from BCE axis). The pressures measured with the sensors at a distance of nearly 6 m from BCE axis transversal to room 213 (open symbols) are not met by the calculation (dashed lines). In general the drilling of boreholes for the measurement of porewater pressure has an influence on the pressure distribution. As long as the boreholes are open they are under atmospheric pressure. In case that drilling and open phase are not included in the modelling sequence – as in the modelling sequence reported here – the calculated pressures in the rock have to deviate from the measured data.

For the depth of 4.6 m from the floor of room 213 (figure 4-24) the calculated values do not agree with the measured data. For the early time data the drilling procedure as mentioned before might have caused the deviations. Later on the thermal pulse might have contributed to the deviation for following reason: The rock has a very low permeability and – more important – porosity. The borehole intervals instead have a high, water filled porosity. The thermal expansion of water is higher than the thermal expansion of the rock, and in combination with the low permeability of the surrounding rock a thermal pulse from the heater causes a pressure pulse in the borehole interval. The figures for the pressure and stress derivatives in the boreholes HG9, HG7, and HG10 (figure 4-26 to figure 4-28) show this phenomenon. Unless the boreholes are modelled with their actual geometries and porosities the thermally caused pressure pulse cannot be captured.

The water pressure evolution in the contact zone of buffer and rock (figure 4-25) is not captured by the calculation. The measured pressures do not indicate a clear pressure distribution which increases towards the bottom of the borehole. The deepest sensor IRH4 shows a value around 180 kPa and the higher sensors IRH1 to IRH3 show uniformly a value around 80 kPa which might be explained by a highly permeable pathway between the sensors. The model in contrast assumes a perfect contact between buffer and rock, therefore the calculated values for sensors IRH2 to IRH4 show a clear increase with depth. The calculated value for the highest sensor IRH1 shows that the contact zone in the model is still not resaturated at the end of test.

The water pressure evolution in the rock around ITT (figure 4-30) is another example for the already mentioned deviation between measurement and calculation in case that the drilling procedure of boreholes is not included into the model. The sensors are located in different distances to the emplacement borehole, and IRP3 has in comparison to IRP2 a longer distance to the buffer contact. Nevertheless the measured values are finally higher for IRP2, and the values for all sensors start at zero (relative) pressure. These observations cannot be captured by a modelling calculation.

The calculated water pressure distribution further into the rock (figure 4-31) shows a good agreement with the measured data, both with respect to the value and with respect to the tendency of development.

The calculated water content distribution in the buffer of BCE at end of test (figure 4-32) shows that large areas of the buffer above the heater remain unsaturated. From top of canister downwards the buffer is fully saturated in the calculation except the immediate vicinity to the heater which shows (extreme) drying occurs in the calculation. The comparing plots for the water content evolution (figure 4-33) can only be interpreted with respect to their tendency: the theoretical maximum of water content with the given values for porosity and (average) grain density is 20.9% (at full saturation). Suction is zero at full saturation. The calculated values remain in that theoretical range, the measured values do not.

The calculated water content distribution in the buffer of ITT at end of test (figure 4-36) shows that the overall water intake is captured by the calculation. The same holds for the water uptake test described in chapter 4.1 which was used for calibration of the hydraulic properties. In comparison to the measured data the calculated saturation front is too steep. This can also be seen in the water content evolution plots (figure 4-37), especially for sensor IBX21.

The calculated total stresses do not agree well with the measured data. The total pressure is governed by swelling pressure which in turn is governed by the water content. A special emphasize in this modelling work was the use of one consistent set of hydraulic parameter values not only for the benchmarks, but also for the water uptake test. The resulting deviations in water content which have been discussed previously therefore influence of course also the total pressure.

# 6 Summary

In 2004 the Swedish Nuclear Fuel and Waste Management Co. (SKB) initiated the project "Task Force on Engineered Barrier Systems". This project has the objectives to verify the ability to model THM-coupled processes (task 1) and gas migration processes (task 2) in the clay-rich buffer materials. The tasks will be performed on the basis of appropriate benchmarks.

This report describes the final results for the modelling of the THM-benchmarks 2.1.1 (Buffer/Container Experiment) and 2.1.2 (Isothermal Test) and also the calibration with a laboratory water uptake test with the code GeoSys/RockFlow. Both in-situ experiments were conducted in the Canadian URL. An interim report (NOWAK 2008) documented the results of two axially symmetric models.

Main reason for the recalculation of these benchmarks was that the calibration with the water uptake test (compare chapter 3.1 and 4.1) was not yet completed. In the modelling work described in this report it was especially featured to use one set of hydraulic parameter values for modelling both the water uptake test and the in-situ experiments. This approach limits the possibilities to match the measured data in the calculation by parameter value fitting.

Further reasons were the development of a new interface from GINA (BGR) to the 3-D mesh generation tool TetGen from the Weierstrass Institute for Applied Analysis and Stochastics (SI & GAERTNER 2005) and the progress made in the parallelization of GeoSys/RockFlow. The benchmarks 2.1.1 and 2.1.2 offered an appropriate test case for field-scale application.

The calculation of thermal processes succeeded very well for benchmark 2.1.1. Deviations to measured data can be attributed to the weathering of the URL which cannot be modelled in an appropriate way without enormous effort.

The overall hydraulic behaviour of the buffer is captured by the models both for the water uptake test and the benchmarks. The calculated saturation fronts are too steep in comparison to measured data, but this mismatch was accepted to keep unity of hydraulic parameter values in all models.

Mechanical processes in the buffer are governed by swelling which in turn depends on the water uptake. In consequence the mismatch in hydraulic behaviour has to be accepted also for the development of total pressure.

To sum up, the modelling work documented in this report demonstrates that GeoSys/RockFlow is capable to perform THM-coupled calculations in 3-D at acceptable computational cost.

# 7 References

**GRAHAM, J., CHANDLER, N. A., DIXON, D. A., ROACH, P. J., TO, T. & WAN, A. W. L.** (1997): The Buffer/Container Experiment: Results, synthesis, issues. - Atomic Energy of Canada Limited, **AECL-11746, COG-97-46-1**.

**KALBACHER, T., WANG, W., WATANABE, N., PARK, C-H., TANIGUCHI, T. & KOLDITZ, O.** (2008): Parallelization concepts and application for THM coupled finite element problems. J Environmental Science and Sustainable Society, vol. 2: 35-46.

**MAAK, P. & SIMMONS, G. R.** (2005): Deep geologic repository concepts for isolation of used fuel in Canada. (In: Proc. of Waste Management, Decommissioning, and Environmental Restoration for Canada's Nuclear Activities - Current Practices and Future Needs. Ottawa, Canada, May 8-11)

**NOWAK, T.** (2007): Modelling of THM-coupled processes for Task 1, Benchmarks 1, using GeoSys/RockFlow. - Svensk Kärnbränslehantering, **IPR-07-13**: 47 p., 30 fig., 3 tab.; Stockholm.

**NOWAK, T.** (2008): Task Force on Engineered Barrier Systems: Modeling of Benchmarks 2.1.1 and 2.1.2. - Federal Institute for Geosciences and Natural Resources, **10116/08**: 49 p., 43 fig., 7 tab.; Hannover.

**SHAO, H. & NOWAK, T.** (2008): DECOVALEX IV - THMC Summary and Achievement. - Federal Institute for Geosciences and Natural Resources, **10075/08**: 148 p.; Hannover.

**SI, H. & GAERTNER, K.** (2005): Meshing Piecewise Linear Complexes by Constrained Delaunay Tetrahedralizations. (In: Proc. of the 14th International Meshing Roundtable, pp. 147-163, September 2005)

**WAN, A. W. L., GRAY, M. N. & GRAHAM, J.** (1995): On the relations of suction, moisture content, and soil structure in compacted clays. (Proc. of the 1st International Conference on Unsaturated Soils, pp. 215-222; Paris).